

EVOLUTION OF A NUCLEAR GAS DISK AND GAS SUPPLY TO THE GALACTIC CENTER. I. MIGRATION OF MASSIVE GAS CLUMPS

DAISUKE NAMEKATA¹ AND ASAO HABE²

¹ Center for Computational Astrophysics, National Astronomical Observatory of Japan, 2-21-1, Osawa, Mitaka, Tokyo 181-8588, Japan; namekata@cfca.jp

² Department of Cosmosciences, Graduate School of Science, Hokkaido University, Sapporo 060-0810, Japan; habe@astro1.sci.hokudai.ac.jp

Received 2010 September 20; accepted 2011 February 14; published 2011 March 23

ABSTRACT

We investigate the gas supply process from a nuclear gas disk to the Galactic center by performing two-dimensional hydrodynamic simulations including self-gravity and radiative cooling. We assume that the gas is supplied to the nuclear gas disk by the host galaxy disk. We show that many gas clumps are formed in the nuclear gas disk after the nuclear gas disk becomes massive enough to become gravitationally unstable. Coalescence of the gas clumps leads to the formation of more massive gas clumps. Gravitational encounters between these massive gas clumps induce angular momentum transfer between the gas clumps. Massive gas clumps that lose their angular momentum due to gravitational encounters move to the galactic center. In this way, the gas supply to the galactic center is realized. We also perform a numerical simulation with twice the spatial resolution to check numerical resolution effects. Time evolution of azimuthally averaged surface density distributions in both models agree well with each other. The high-mass part of the clump mass function in the low-resolution model is in good agreement with that of the high-resolution model, and lower mass clumps are well resolved in the high-resolution model. Therefore, we conclude that massive gas clumps play a major role in the angular momentum transfer. The gas supply rate to the center is about half of the gas supply rate from the host galaxy when the whole region of the nuclear gas disk becomes self-gravitationally unstable. More massive gas clumps are formed and migrate to the Galactic center in the models of the higher gas supply rate from the host galaxy.

Key words: Galaxy: center – Galaxy: kinematics and dynamics – methods: numerical

Online-only material: color figures

1. INTRODUCTION

Gas supply to galactic centers is important for activity in galactic centers and growth of super-massive black holes (SMBHs). Our Galaxy is a very good object for the study of the process of gas supply to galactic centers for the following reasons: First, the center of our Galaxy is the closest galactic center. Its distance is about 8.0 kpc from us (Eisenhauer et al. 2003). Therefore, there are many observational data with high resolution over multiple wavelengths. Second, there is an SMBH whose mass is about $(4.0\text{--}4.5) \times 10^6 M_\odot$ at the Galactic center (Ghez et al. 2008; Gillessen et al. 2009a, 2009b). Third, there is evidence of recent gas supply and massive star formation in the last several Myr.

In the following, we summarize observational features related to recent mass supply and active star formation in the central region of our Galaxy. The center of our Galaxy is buried in a massive and dense gas region ($M_{\text{gas}} \sim 5.0 \times 10^7\text{--}10^8 M_\odot$) called the central molecular zone (CMZ; Serabyn & Morris 1995; Morris & Serabyn 1996). The size of the CMZ is ~ 400 pc. The CMZ can be formed by the large-scale stellar bar in our Galaxy (Binney et al. 1991; Sawada et al. 2004). Inside of the CMZ, there is evidence of active star formation within the last several Myr. At the projection radius of about 120 pc from the Galactic center, there is the Sagittarius B2 molecular cloud, which contains many young stars (Gaume et al. 1995). At the projection radius of about 30 pc from the Galactic center, there are two massive compact young star clusters, the Arches cluster and the Quintuplet cluster (Figer et al. 1999). These star clusters have significant impact on the surrounding interstellar medium through stellar winds and intense ionizing photon flux (Figer 2003). There is also a young star cluster around Sgr A*, the

central cluster (Genzel et al. 2003). These clusters have masses of $\sim 10^4 M_\odot$ and contain hundreds of massive stars (Figer et al. 1999). The concentration of massive stars just within 30 pc requires a vast amount of gas to flow into these regions in a short-timescale for this star formation event.

There are observations of a large amount of molecular gas within the central 10 pc (Mezger et al. 1996; Coil & Ho 1999, 2000; McGray et al. 2001; Wright et al. 2001; Herrnstein & Ho 2002, 2003, 2005; McGray & Ho 2002; Lee et al. 2003, 2008; Shukla et al. 2004; Christopher et al. 2005; Donovan et al. 2006). A molecular gas ring called the circumnuclear disk (CND) surrounds Sgr A*. The radius of the CND is 2–5 pc and its mass is estimated to be $3 \times 10^5\text{--}10^6 M_\odot$ (Shukla et al. 2004; Christopher et al. 2005; Montero-Castaño et al. 2009). The average density of the gas in the CND is about 10^5 cm^{-3} , and the internal motion is very turbulent (the typical full width half-maximum (FWHM) of line profiles of molecular emissions in the CND is $\sim 40 \text{ km s}^{-1}$; Coil & Ho 1999). Around the CND, there are two large molecular clouds, the 50 km s^{-1} cloud and the 20 km s^{-1} cloud. Coil & Ho (1999) discovered a molecular gas streamer connected from the 20 km s^{-1} cloud to the eastern side of the CND, which may be a signature of the recent gas supply. It is very important to study how such gas supply processes occur in our Galaxy in order to understand the evolution of the Galactic center.

What mechanism drives a vast gas supply to the central region of our Galaxy? Several possible mechanisms have been proposed (e.g., Wada & Habe 1992; Lee et al. 1999; Fukunaga & Tosa 1989b; Shlosman et al. 1989). Wada & Habe (1992) showed the importance of self-gravity of gas in the mass supply process from the galactic disk to the galactic center by numerical simulation of self-gravitating gas in a

weak-barred galaxy. Lee et al. (1999) performed smoothed particle hydrodynamics (SPH) simulations to study the response of molecular clouds in the Galactic disk to a rotating large-scale bar and their subsequent evolution in the Galactic center region. They estimated the inflow rate of gas within 1 kpc to be about $0.1\text{--}0.3 M_{\odot} \text{ yr}^{-1}$. However, they employed a small number of SPH particles ($<10,000$) and did not consider self-gravity of gas.

In our recent paper (Namekata et al. 2009, hereafter Paper I), we studied the possibility of gas supply by the inner bar, evidence of which is given by recent observations (Alard 2001; Nishiyama et al. 2005, 2006). The inner bar is nested in the large-scale bar of our Galaxy. Such structures are often called “nested bars.” Gas fueling by nested bars was first proposed by Shlosman et al. (1989) to explain the growth of SMBHs. Many numerical and observational studies have been performed (Buta & Crocker 1993; Shaw et al. 1993; Friedli & Martinet 1993; Friedli 1996; Maciejewski & Sparke 1997, 2000; Heller et al. 2001; Erwin & Sparke 2002; Shlosman & Heller 2002; Rautiainen et al. 2002; Maciejewski et al. 2002; El-Zant & Shlosman 2003; Erwin 2004; Englmaier & Shlosman 2004; Heller et al. 2007; Debattista & Shen 2007; Shen & Dibattista 2009). Recent observations show that one-third of early-type nearby spiral galaxies have nested bars (Erwin & Sparke 2002).

In Paper I, we investigated the gas supply process to the central region of our Galaxy by nested bars using high-resolution hydrodynamical simulations, assuming various sizes and ratios of inner bars. We showed that gas supply occurs from the CMZ through two stream inflows that are realized in the nested bars, and a nuclear gas disk is formed by the gas supply. The radius of the nuclear gas disk is comparable to radial distances of the young clusters observed in the Galactic center. A nuclear gas disk much smaller than 15 pc is not obtained without destroying the CMZ. The size of the nuclear gas disk is close to the location of the young clusters observed in our Galactic center. The mass of the nuclear gas disk can reach $\sim 10^6\text{--}10^7 M_{\odot}$ by the gas supplied by the nested bars, and the gas supply rate is $\sim 0.1 M_{\odot} \text{ yr}^{-1}$. We also showed using linear perturbation analysis that the nuclear gas disk in this stage is self-gravitationally unstable. Very high resolution numerical simulations that can resolve gravitational instability of the nuclear gas disk are needed to investigate further evolution of the nuclear gas disk, including clump formation and star formation.

In this study and subsequent papers, we investigate the gas supply process from the nuclear gas disk obtained in Paper I to the Galactic center, and evolution of the nuclear gas disk using hydrodynamical/ N -body simulations. In this paper, we perform two-dimensional hydrodynamical simulations of the nuclear gas disk in order to focus on hydrodynamic effects. We will investigate the effects of star formation and stellar feedbacks such as supernova, stellar wind, and FUV radiation from massive stars in subsequent papers.

This paper is organized as follows: In Section 2, we describe our models and our numerical code in detail. In Section 3, we show the results of our numerical simulations. In Section 4, we discuss star formation in the nuclear gas disk, the effects of star formation on the gas supply process, the formation of the CND, and the statistical properties of the gas clumps in the nuclear gas disk. In Section 5, we summarize our study.

2. MODEL AND NUMERICAL METHODS

2.1. Model

In order to investigate the process of gas supply from the nuclear gas disk to the Galactic center, we perform numerical simulations of the nuclear gas disk in two dimensions, treating gravitational potential of our Galaxy as external gravity and assuming gas supply from the host galaxy to the nuclear gas disk. We assume that the initial nuclear gas disk extends 5–15 pc in radius and is self-gravitationally stable. To mimic the two stream inflows that supply gas to the nuclear gas disk found in Paper I, we assume two gas sources at $(\pm 30 \text{ pc}, 0 \text{ pc})$ whose positions are fixed during the simulations for simplicity, and that the supplied gas has the same specific angular momentum of a circularly rotating gas at $R = 17.5 \text{ pc}$. This value of the specific angular momentum is large enough to avoid change in the size of the nuclear gas disk and is appropriate to realize a smooth gas flow connecting from the gas sources to the outer edge of the nuclear gas disk without strong disturbance. By the gas supply from the host galaxy, gas in the outer part of the nuclear gas disk will become self-gravitationally unstable at some stage of the simulation. We expect that gas clumps form via the self-gravitational instability in the nuclear gas disk. To follow gas clump formation and angular momentum transfer via their mutual gravitational interaction, we perform two-dimensional hydrodynamic simulations, taking into account the self-gravity of the gas and radiative cooling.

We assume an external gravitational potential of the nuclear region of our Galaxy using the mass distribution derived by Launhardt et al. (2002), who analyzed *IRAS*³ and *COBE*⁴/*DIRBE*⁵ data of the central 500 pc of our Galaxy assuming a constant mass-to-light ratio. They gave mass distribution of the nuclear bulge, which is distinguished from the Galactic bulge by its flat disk-like feature. They estimated that the mass of the nuclear bulge is $(1.4 \pm 0.6) \times 10^9 M_{\odot}$. We do not assume the inner and outer bars in this paper. We have checked that the gravity of both bar components does not affect numerical results of the evolution of the nuclear gas disk. The SMBH dominates the gravitational potential within 1 pc and the nuclear star cluster dominates at radii $>1 \text{ pc}$. Assuming a spherical mass distribution, we obtain the rotation curve and the angular frequency curve as shown in Figure 1. Figure 1 shows that the rotation velocity is almost flat in our simulation region. The steep rise of the rotation curve near $R = 0 \text{ pc}$ is due to the gravity of the SMBH.

In order to investigate the effects of the gas supply rate from the host galaxy, we simulate three cases of the gas supply rate from the host galaxy, $\dot{M}_{\text{host}} = 0.01, 0.05, \text{ and } 0.1 M_{\odot} \text{ yr}^{-1}$, since we expect that the evolution of the nuclear gas disk affects the gas supply process from the nuclear gas disk to the Galactic center and depends on \dot{M}_{host} . These values are in the range of time-averaged gas supply rates obtained in Paper I, in which we studied the gas supply process assuming nested bars in our Galaxy. We name these models *M0.01*, *M0.05*, and *M0.1* corresponding to $\dot{M}_{\text{host}} = 0.01, 0.05, \text{ and } 0.1 M_{\odot} \text{ yr}^{-1}$, respectively.

In the process of gas supply to the galactic center, the shear velocity field in the nuclear gas disk is very important, since migration of massive gas clumps is induced by their angular

³ The *Infrared Astronomical Satellite*.

⁴ The *Cosmic Background Explorer*.

⁵ The Diffuse Infrared Background Experiment.

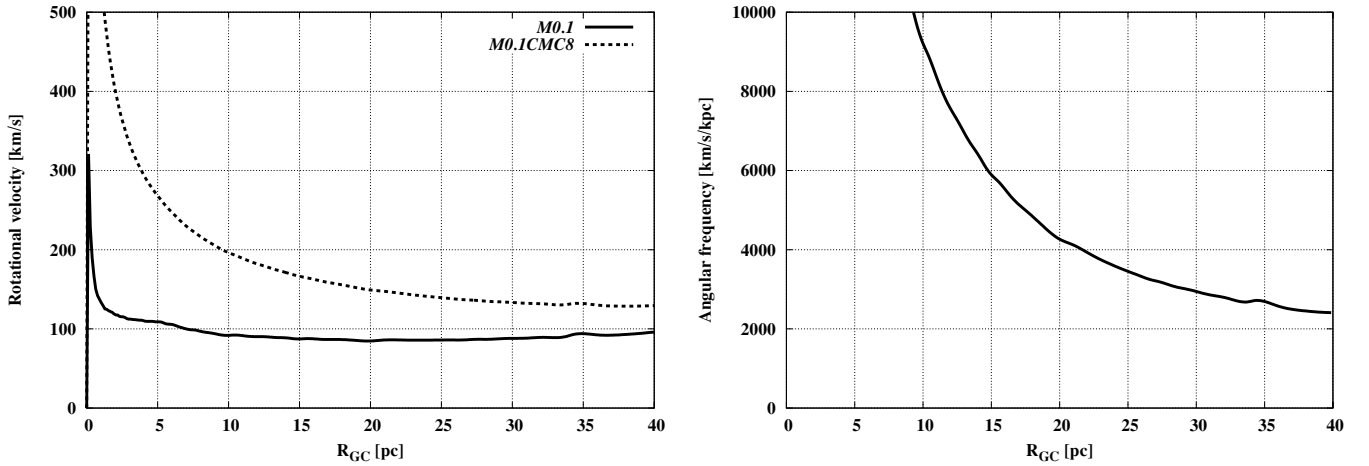


Figure 1. Rotation curve (left panel) and angular frequency curve (right panel). The horizontal axis shows the radius from the galactic center.

Table 1
Numerical Models

Model Name	$\dot{M}_{\text{host}} (M_{\odot} \text{ yr}^{-1})$	Description
<i>M0.01</i>	0.01	...
<i>M0.05</i>	0.05	...
<i>M0.05s</i>	0.05	The gas supply till $t = 24$ Myr.
<i>M0.1</i>	0.1	...
<i>M0.1s</i>	0.1	The gas supply till $t = 12$ Myr.
<i>M0.1d</i>	0.1	The direct gas supply to the outer edge of the nuclear gas disk.
<i>M0.1CMC8</i>	0.1	$M_{\text{SMBH}} = 10^8 M_{\odot}$
<i>M0.1hr</i>	0.1	The high-resolution version of <i>M0.1</i>

momentum transfer due to the mutual gravitational interaction. We perform a numerical simulation for the more massive SMBH of $10^8 M_{\odot}$ (model *M0.1CMC8*) as a strong shear velocity case. In this simulation, we assume the gravitational softening of 0.25 pc for the SMBH. The gravitational softening is introduced to avoid too small time steps around the SMBH. We show the rotation curve of this model by the dotted line in the left panel of Figure 1.

We find that the angular momentum in the nuclear gas disk is redistributed by gravitational encounters between gas clumps. The gas supply to inner radii may depend on the size and mass of gas clumps. These may depend on the spatial resolution. To check the effects of the spatial resolution, we perform a numerical simulation with high resolution (model *M0.1hr*). The grid number of this model is 1215^2 and the corresponding spatial resolution is 0.065 pc. We summarize our numerical models in Table 1.

2.2. Initial Condition

We use 625^2 Cartesian grid points for the $80 \text{ pc} \times 80 \text{ pc}$ region in the Galactic center. The corresponding numerical resolution is 0.128 pc. This is enough to resolve a small (~ 1 pc) molecular cloud. Initially, we assume a self-gravitationally stable nuclear gas disk whose inner and outer radii are 5 pc

and 15 pc, respectively. The size of the nuclear gas disk is based on the results of Paper I. The nuclear gas disk is rotationally supported against the gravitational force of the host galaxy and the self-gravity of the gas and is immersed in high-temperature rarefied gas. We uniformly add the density fluctuation of 1% amplitude on the nuclear gas disk. The numerical simulations are performed for 48 Myr except for models *M0.01* and *M0.1hr*. Models *M0.01* and *M0.1hr* are performed for 120 Myr and 30 Myr, respectively. These simulation times are long enough to follow dynamic evolution of the nuclear gas disk, since the rotational period at $R = 10$ pc is ≈ 0.6 Myr, which is much shorter than the simulation time.

2.3. Numerical Methods

2.3.1. Basic Equations

The basic equations are

$$\frac{\partial \rho}{\partial t} + \nabla \cdot (\rho \mathbf{v}) = \dot{\rho}_s, \quad (1)$$

$$\frac{\partial (\rho \mathbf{v})}{\partial t} + \nabla \cdot (\rho \mathbf{v} \mathbf{v}) = -\nabla p - \rho \nabla (\Phi_{\text{ext}} + \Phi_{\text{self}}) + \frac{\partial}{\partial t} (\rho_s \mathbf{v}_s), \quad (2)$$

$$\begin{aligned} & \frac{\partial}{\partial t} \left\{ \rho \left(\frac{1}{2} \mathbf{v}^2 + e \right) \right\} + \nabla \cdot \left\{ \rho \mathbf{v} \left(\frac{1}{2} \mathbf{v}^2 + h \right) \right\} \\ & = -\rho \mathbf{v} \cdot \nabla (\Phi_{\text{ext}} + \Phi_{\text{self}}) + \Gamma - \Lambda + \frac{\partial}{\partial t} (\rho_s E_s), \end{aligned} \quad (3)$$

$$p = \frac{\rho k_B T}{\mu m_H}, \quad (4)$$

$$\Delta \Phi_{\text{self}} = 4\pi G \rho, \quad (5)$$

where ρ is the density of the gas, \mathbf{v} is its velocity, and p is its thermal pressure. Φ_{ext} is the external gravitational potential; Φ_{self} is the self-gravitational potential; e is the specific internal energy; h is the specific enthalpy; G is the gravitational constant; T is the thermal temperature; k_B is the Boltzmann constant; μ is the mean molecular weight in the unit of m_H , which is the mass of atomic hydrogen; Γ is the heating function; Λ is the cooling function; and $\dot{\rho}_s$, $\dot{\mathbf{v}}_s$, and \dot{E}_s are the source terms corresponding to the gas supply from the host galaxy.

2.3.2. Hydrodynamics

We numerically solve the hydrodynamic equations by the M-AUSMPW⁺ (Kim & Kim 2005b) with the MLP5 (Kim & Kim 2005a). The M-AUSMPW⁺, which is one of the advection upstream splitting method (AUSM) type schemes, is more robust than the previous AUSM-type schemes such as AUSM and AUSM⁺, owing to an introduction of pressure-based weight functions, and has high spatial accuracy in smooth regions of a flow. The combination of the M-AUSMPW⁺ with the MLP5 enhances numerical stabilities in multi-dimensional flows. The M-AUSMPW⁺ and the MLP5 are summarized in Appendices A and B.

2.3.3. Self-gravity

The self-gravity of the gas is calculated by solving the Poisson equation. We use the convolution method (Hockney & Eastwood 1988) with the fast Fourier transform (FFT) to solve the Poisson equation. In this study, we use the FFTW library⁶ for the FFT. We use the isolated boundary condition.

2.3.4. Time Step and Time Integration Method

We determine the time step Δt as the following:

$$\Delta t = \min(\Delta t_{\text{CFL}}, \Delta t_{\text{G}}), \quad (6)$$

$$\Delta t_{\text{CFL}} = \min_{i,j} C_{\text{CFL}} \times \min \left(\frac{\Delta x}{|u_{i,j}| + c_{s,i,j}}, \frac{\Delta y}{|v_{i,j}| + c_{s,i,j}} \right), \quad (7)$$

$$\Delta t_{\text{G}} = \min_{i,j} 0.333 \sqrt{\frac{\min(\Delta x, \Delta y)}{\max(|g_{x,i,j}|, |g_{y,i,j}|)}}, \quad (8)$$

where $\Delta x, \Delta y$ are the mesh sizes for each direction, $\mathbf{v}_{i,j} = (u_{i,j}, v_{i,j})$ is the velocity of gas, $c_{s,i,j}$ is the sound speed of gas, C_{CFL} is the Courant–Friedrich–Lewy (CFL) number, and $\mathbf{g}_{i,j} = (g_{x,i,j}, g_{y,i,j})$ is the gravitational force. We adopt $C_{\text{CFL}} = 0.1$.

We use the second-order total variation diminishing (TVD) Runge–Kutta method for the integration of the hydrodynamic equations. This is written as

$$u^{(1)} = u^n + \Delta t L(u^n), \quad (9)$$

$$u^{n+1} = \frac{1}{2}u^n + \frac{1}{2}u^{(1)} + \frac{1}{2}\Delta t L(u^{(1)}), \quad (10)$$

where L is the operator given in the right-hand side of the Equation (A7) (Shu 1988).

2.3.5. Cooling and Heating Processes

We use the cooling function given by Spaans & Norman (1997), who derived the cooling functions for various metallicities of gas. We assume the solar metallicity. In our numerical calculation, we use our analytical cooling formula by fitting the procedure to speed up the calculation of the cooling rate. In Figure 2, we show our cooling function.

We assume a uniform far-ultraviolet (FUV) radiation field and cosmic-ray heating as heating sources. We assume the FUV radiation field given by Gerritsen & Icke (1997),

$$\Gamma_{\text{FUV}} = 1 \times 10^{-24} \epsilon G_0 \text{ erg cm}^{-3} \text{ s}^{-1}, \quad (11)$$

where ϵ is the heating efficiency and G_0 is the incident FUV field normalized to the local interstellar value given by Habing (1968). We assume $\epsilon = 0.05$ and $G_0 = 1$. For cosmic-ray heating, we adopt the heating rate given by Yusef-Zadeh et al. (2007). They derived the rate of the cosmic-ray heating from the distribution of K_α 6.4 keV Fe line emission in the Galactic central region as

$$\Gamma_{\text{CR}} = 3 \times 10^{-24} n_{\text{H}} \text{ erg cm}^{-3} \text{ s}^{-1}, \quad (12)$$

where n_{H} is the number density of the atomic hydrogen.

In our simulation, we integrate the internal energy equation after the time integration of the hydrodynamic part,

$$\frac{dE_{\text{th}}}{dt} = \Gamma(\rho, T) - \Lambda(\rho, T), \quad (13)$$

where $E_{\text{th}} = \rho e$, Γ is the heating rate per volume, and Λ is the cooling rate per volume. The time integration is performed by the fourth-order Runge–Kutta method with adaptive step size control (Press et al. 1992).

3. NUMERICAL RESULTS

3.1. Model M0.01

We show the time evolution of model *M0.01* in Figure 3. Mass of the nuclear gas disk gradually increases with time for the gas supply. It becomes self-gravitationally unstable in the outer part of the nuclear gas disk. Gas clumps begin to form in the region. These gas clumps gravitationally and hydrodynamically interact with each other. Some clumps begin to move inward due to angular momentum transfer by these interactions. In this way, gas clumps supply their mass to smaller radii in the nuclear gas disk. During the process, the gas clumps are elongated by the strong tidal force of the central compact mass (the SMBH and the nuclear star cluster) and form many transient gas spirals. A small gas disk with high surface density ($\sim 10^4 M_\odot \text{ pc}^{-2}$) is formed within 5 pc in the late simulation stage as shown in the right bottom panel of Figure 3. Hereafter, we call such a disk the central mini disk. The gas distribution in the nuclear gas disk is highly non-uniform and filamentary as shown in the right panels of Figure 3.

The azimuthally averaged surface density of gas $\bar{\Sigma}_{\text{gas}}(R)$ is useful in showing evolution of the nuclear gas disk, where R is the galactic radius. We obtain $\bar{\Sigma}_{\text{gas}}(R)$ in concentric rings with equally spaced width $\Delta r = 0.4 \text{ pc}$. The total number of rings is 100. We show the time evolution of $\bar{\Sigma}_{\text{gas}}(R)$ of model *M0.01* in Figure 4. In this figure, we also show the critical surface densities $\Sigma_{\text{crit}}(R, T_{\text{eff}})$ for three gas effective temperatures that represent the thermal energy and turbulent energy of gas. $\Sigma_{\text{crit}}(R, T_{\text{eff}})$ is given by the linear perturbation stability analysis of a thin gas disk in the tight-winding approximation (Binney & Tremaine 1987). The critical surface density is given as

$$\Sigma_{\text{crit}}(R, T_{\text{eff}}) = \frac{c_s(T_{\text{eff}})\kappa(R)}{\pi G}, \quad (14)$$

where $\kappa(R)$ is the epicyclic frequency and $c_s(T_{\text{eff}})$ is the sound speed of gas with effective temperature, T_{eff} . A hydrostatic gas disk with $\Sigma(x, y) > \Sigma_{\text{crit}}(R, T)$ is locally self-gravitationally unstable. Gas temperature in the dense regions of the nuclear gas disk is less than 100 K in the model. $\bar{\Sigma}_{\text{gas}}(R)$ lies between $\Sigma_{\text{crit}}(R, 10)$ and $\Sigma_{\text{crit}}(R, 100)$. This indicates that the nuclear gas disk is mainly supported by thermal pressure.

⁶ <http://www.fftw.org>

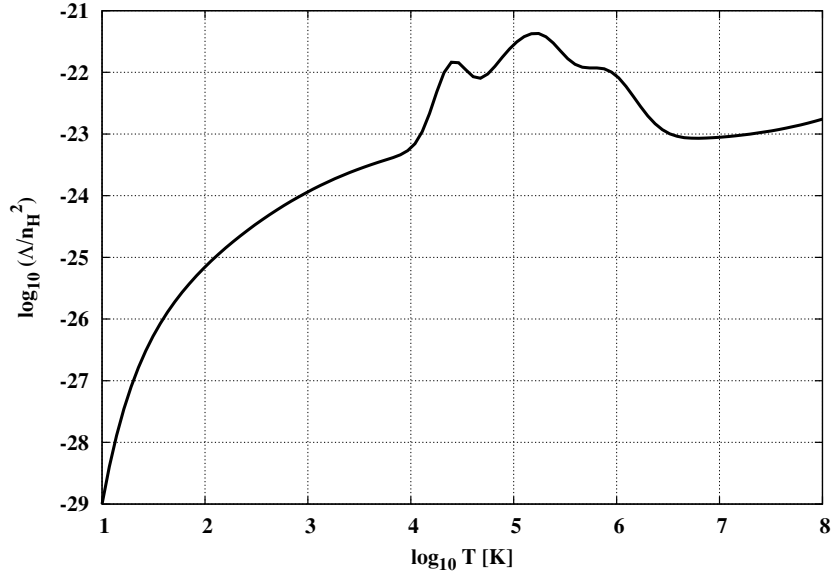
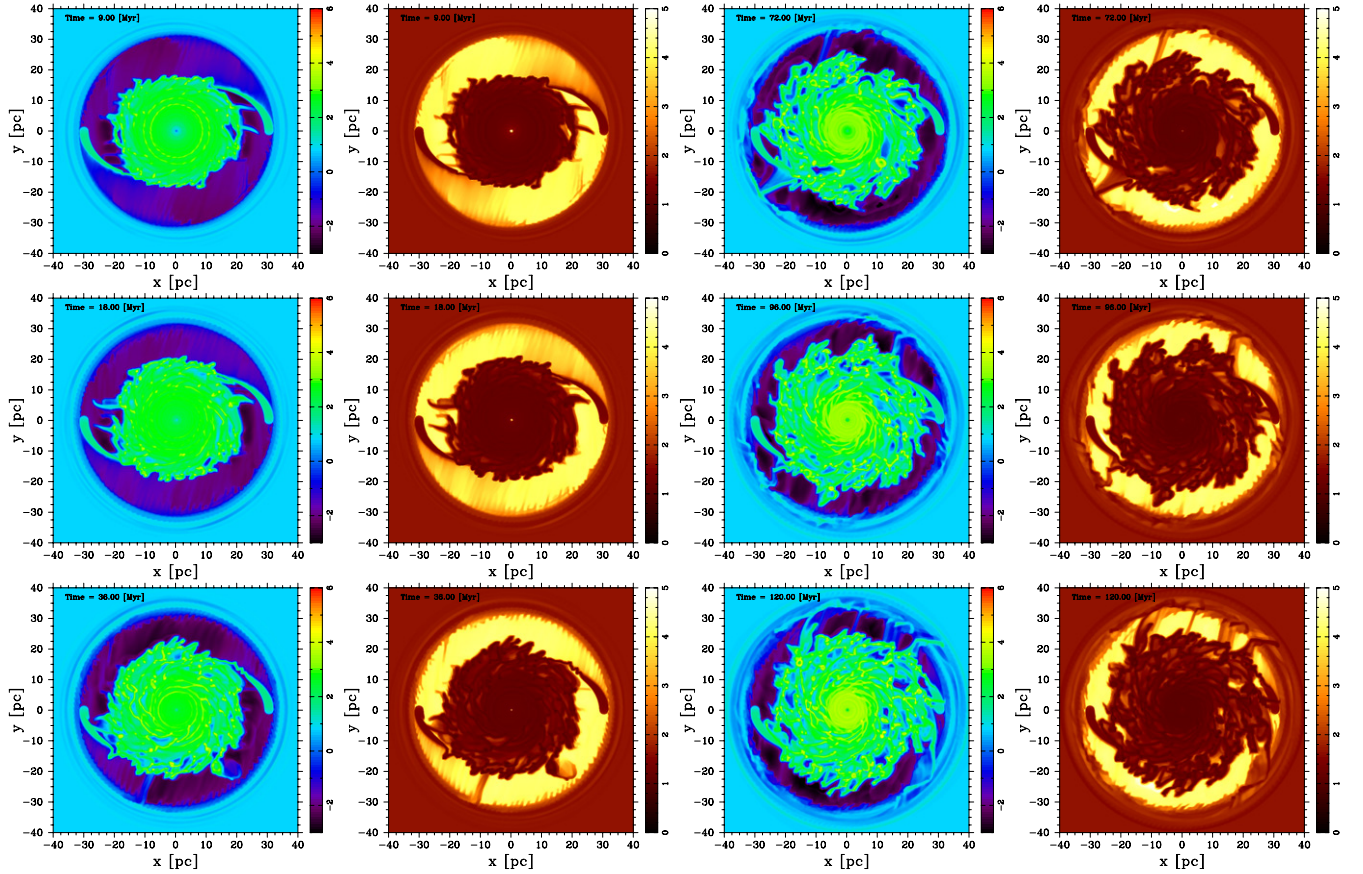


Figure 2. Profile of the analytical cooling formula.

Figure 3. Time evolution of model *M0.01*. The calculation times are shown in the upper left corners of each panel. Colors in both panels show $\log_{10} \Sigma / M_{\odot} \text{ pc}^{-2}$ and $\log_{10} T$, respectively.

(A color version of this figure is available in the online journal.)

3.2. Model *M0.05*

We show the time evolution of model *M0.05* in Figure 5. As in model *M0.01*, the nuclear gas disk begins to be self-gravitationally unstable in the outer part as shown in the left upper panel of Figure 5. Since \dot{M}_{host} of this model is larger than that of model *M0.01*, gas clumps form more rapidly.

Coalescence of the gas clumps occurs in the outer part of the nuclear gas disk and forms very massive gas clumps, e.g., $M_{\text{clump}} \sim 10^4 M_{\odot}$. There are frequently strong gravitational encounters between massive gas clumps. Through the encounters, the angular momentum is strongly exchanged. As a result, some gas clumps are scattered to quite large radii, e.g., 10 pc

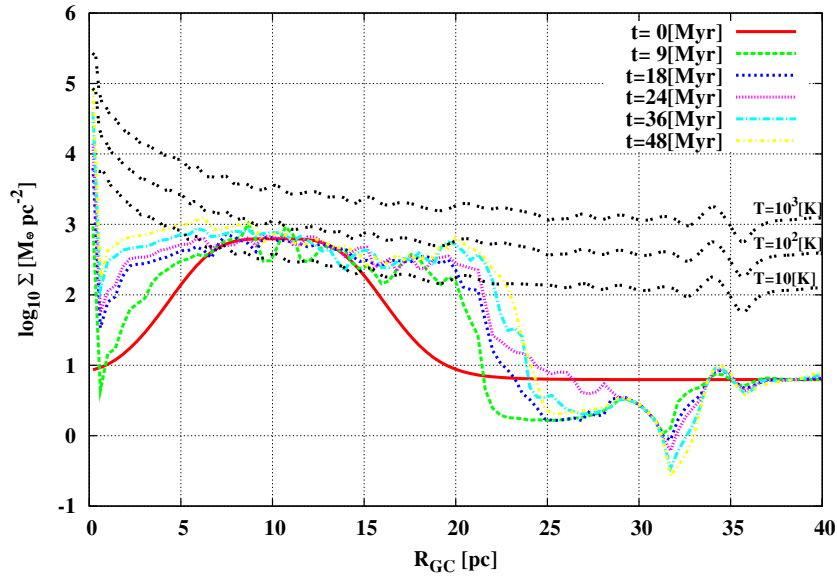


Figure 4. Time evolution of the azimuthally averaged gas surface density in model *M0.01*. The black dotted lines show the critical surface densities, which correspond to the Toomre instability at $T_{\text{eff}} = 10$ K, 100 K, and 1000 K, respectively.

(A color version of this figure is available in the online journal.)

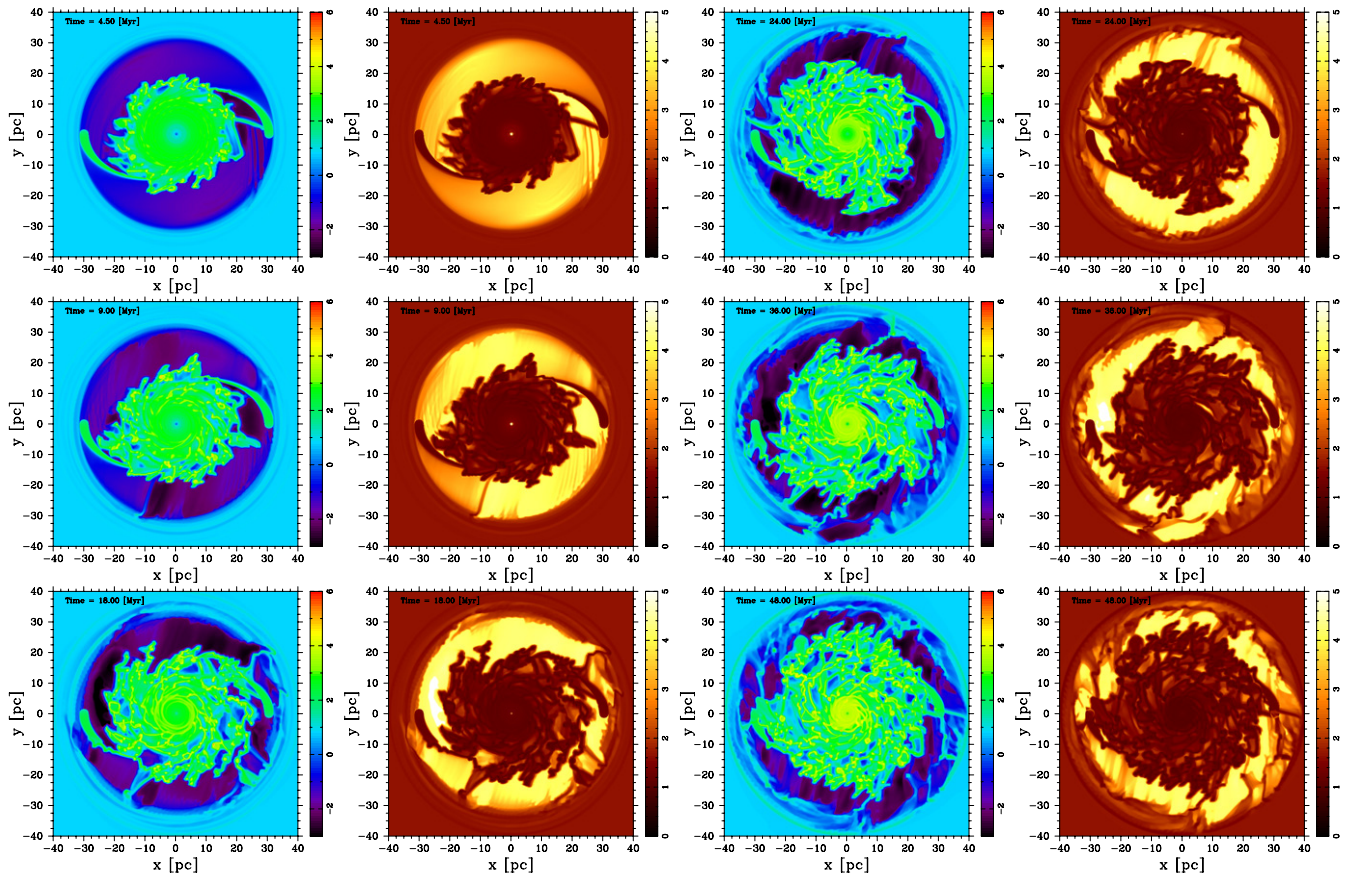


Figure 5. Time evolution of model *M0.05*. The figures in the upper left corners of each panel and the colors are the same as in Figure 3.

(A color version of this figure is available in the online journal.)

outward from the original position. On the other hand, other massive gas clumps move to the inner radii due to the angular momentum transfer without disruption by the tidal force. As in model *M0.01*, the central mini disk forms within 5 pc, as shown in the right middle panel of Figure 5.

Figure 6 shows the time evolution of $\overline{\Sigma_{\text{gas}}}(R)$. The averaged surface densities are around the critical surface density of $T_{\text{eff}} = 100$ K. The effective gas temperature is larger than that of model *M0.01*, since the turbulent motion in this model is more active than that in model *M0.01*. The high

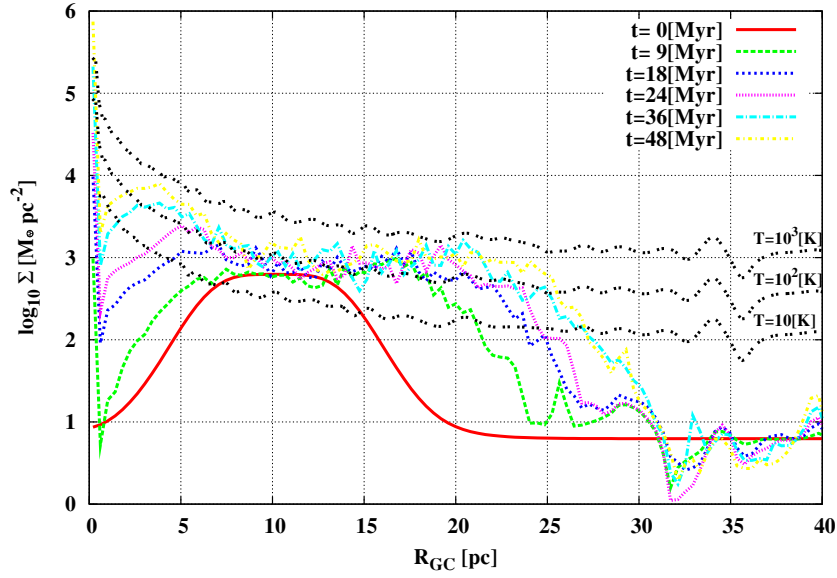


Figure 6. Time evolution of the azimuthally averaged surface density in model *M0.05*. The black dotted lines are the same as in Figure 4. (A color version of this figure is available in the online journal.)

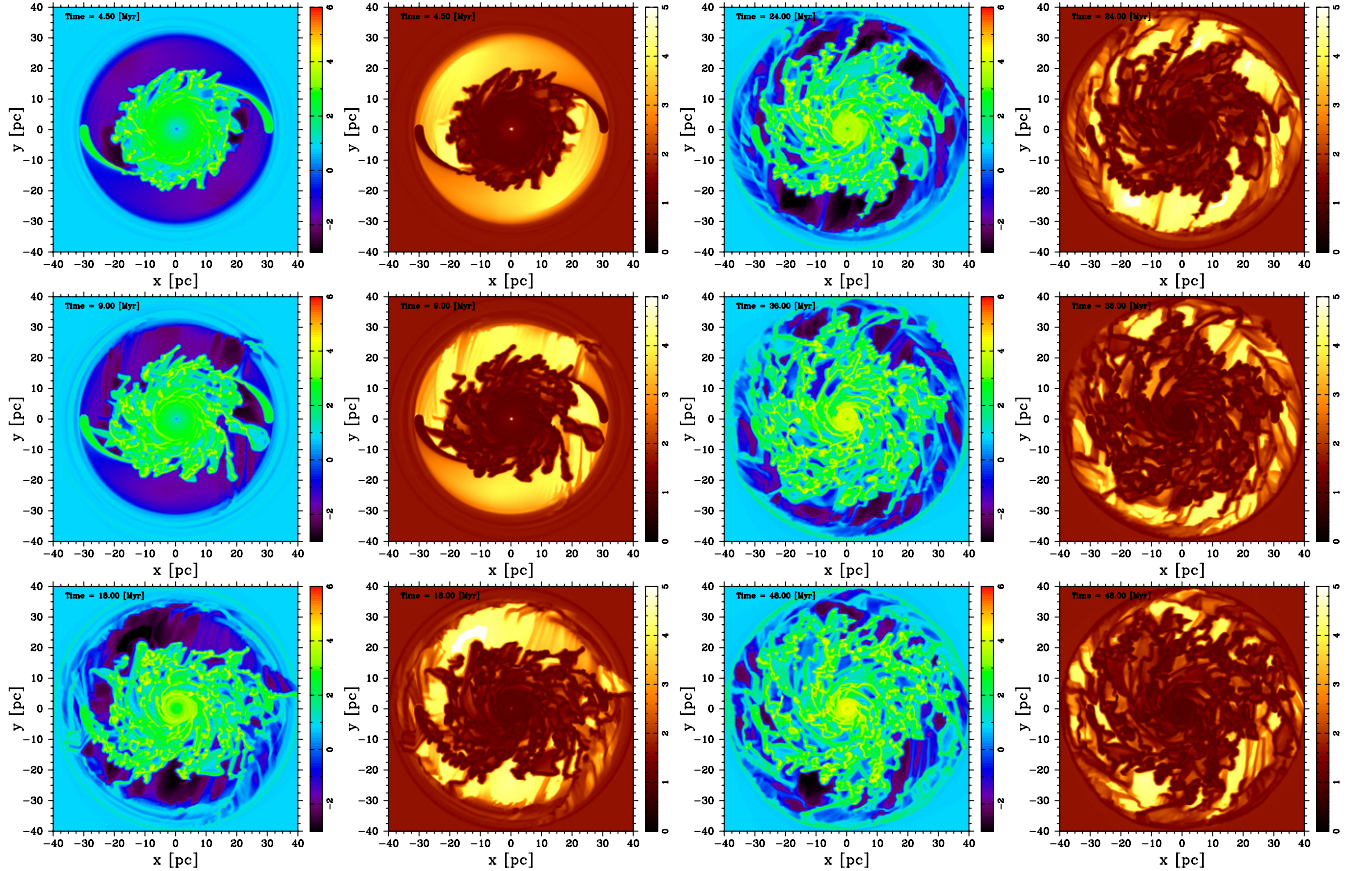


Figure 7. Time evolution of model *M0.1*. The figures in the upper left corners of each panel and the colors are the same as in Figure 3. (A color version of this figure is available in the online journal.)

effective temperature is due to the higher \dot{M}_{host} than in model *M0.01*.

3.3. Model *M0.1*

In this model, we assume a higher mass supply rate than in the previous models. We show the time evolution of model *M0.1*

in Figure 7. In this model, gas clumps form more rapidly than in models *M0.01* and *M0.05*. This is due to the high gas supply rate from the host galaxy. Motions of the gas clumps are highly irregular because of their mutual gravitational interaction. As a result, the nuclear gas disk is more turbulent than in the previous two models.

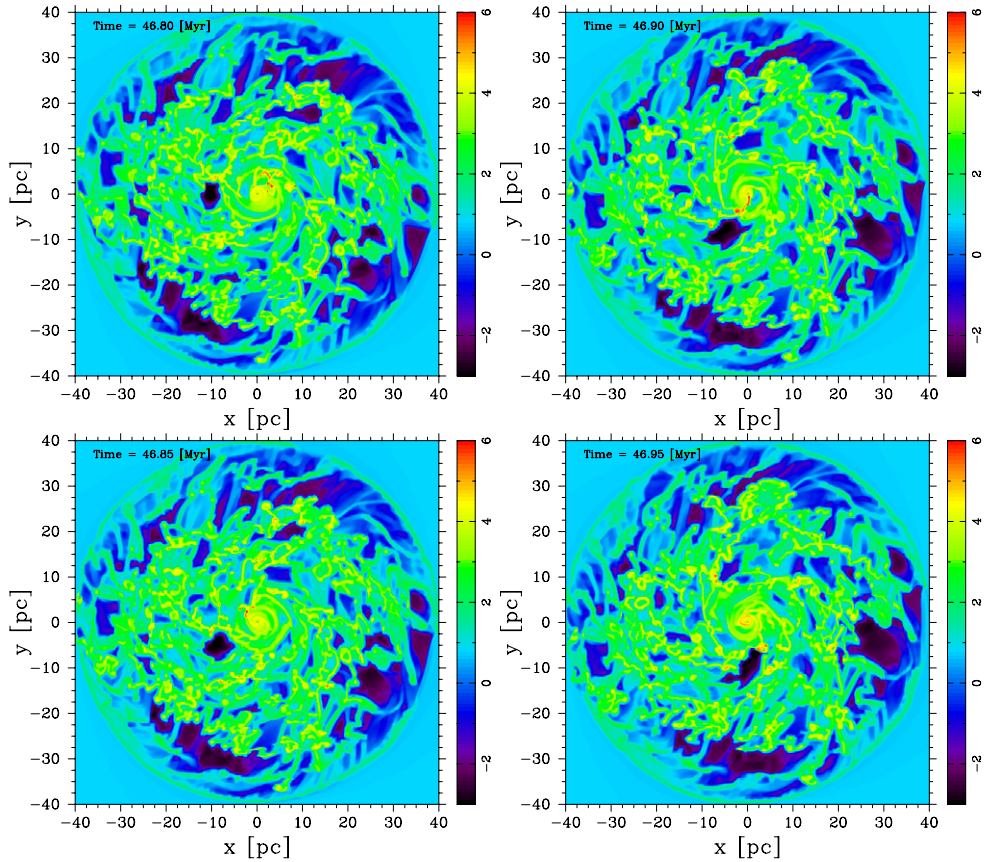


Figure 8. Time evolution of the gaseous surface density in model *M0.1* from $t = 46.80$ – 46.95 Myr. We can see that a massive gas clump migrates to the galactic center.

(A color version of this figure is available in the online journal.)

In this model, a massive gas clump directly migrates to the galactic center. We show one example in Figure 8. At $t = 46.80$ Myr, many massive gas clumps gravitationally interact with each other. Three very massive gas clumps are formed by the coalescence of the gas clumps at $t = 46.85$ Myr. One of these loses its angular momentum by the gravitational encounter and begins to migrate toward the galactic center at $t = 46.90$ Myr. At the same time, the other two clumps coalesce into a more massive clump. At $t = 46.95$ Myr, the falling gas clump is disrupted by the strong tidal force of the central compact mass and spirals in toward the galactic center. The other clump moves outward, since this clump obtains excess angular momentum. Thus, the gas supply to the galactic center is realized by the direct migration of the massive gas clumps that are formed near the galactic center ($R < 10$ pc). The typical migration timescale of massive gas clumps is less than 1 Myr after they form.

Figure 9 shows the time evolution of $\overline{\Sigma_{\text{gas}}}(R)$. Each surface density profile is above the profile of $\Sigma_{\text{crit}}(R, 100)$. This also suggests that the effective gas temperature is enhanced by the turbulent motion. Namely, the gas disk is supported by both the thermal pressure and the turbulent ram pressure. In this model, the tail of the surface density extends to larger radii than in the previous two models. This shows that a vigorous angular momentum transfer occurs in this model.

3.4. Clump Mass Function in Models *M0.1* and *M0.1hr*

We perform a numerical simulation with high resolution to check the effect of the numerical resolution. In Figure 10, we

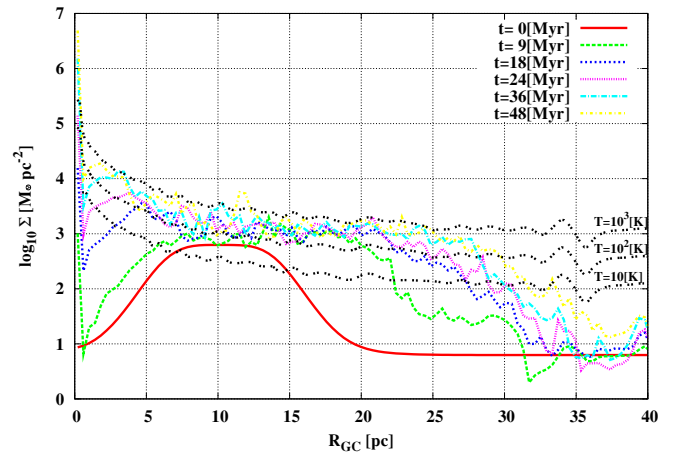


Figure 9. Time evolution of the azimuthally averaged surface density of model *M0.1*. The black dotted line are the same as in Figure 4.

(A color version of this figure is available in the online journal.)

show the time evolutions of $\overline{\Sigma_{\text{gas}}}(R)$ of models *M0.1* and *M0.1hr*. Both results agree well with each other. Therefore, the angular momentum transfer and the gas supply process to the galactic center are well followed in the simulations of model *M0.1* (the resolution of 625^2).

We compare clump mass functions (CMFs) in both models. The clump identification method is described in Appendix C. The CMF at $t = 27.5$ Myr is shown in Figure 11. In model *M0.1hr*, there are many low-mass clumps with

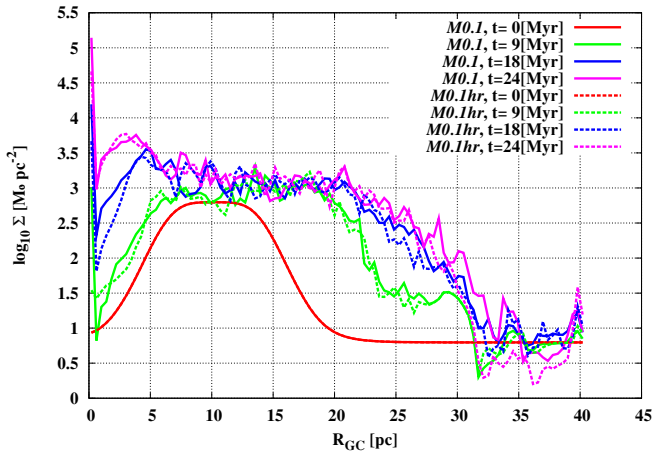


Figure 10. Time evolution of the azimuthally averaged surface density in models *M0.1* and *M0.1hr*.

(A color version of this figure is available in the online journal.)

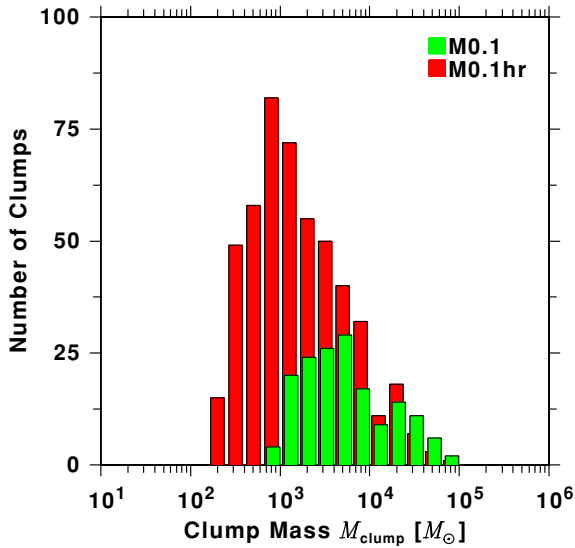


Figure 11. Clump mass function in models *M0.1* and *M0.1hr* at $t = 27.5$ Myr. We slightly offset the columns of model *M0.1* rightward.

(A color version of this figure is available in the online journal.)

$M < 10^4 M_\odot$ because of the high resolution. The peak of the CMF in this model is $\lesssim 10^3 M_\odot$. This is close to the critical mass $M_C = \pi \Sigma_{\text{gas}} \lambda_{\text{max}}^2 / 4$, where λ_{max} is the most rapidly growing unstable wavelength in the Toomre instability, $\lambda_{\text{max}} = 2[c_s(T_{\text{eff}})]^2 / (G \Sigma_{\text{gas}})$. At $\Sigma_{\text{gas}} = 10^3 M_\odot \text{pc}^{-2}$ and $c_s(T_{\text{eff}}) = 1.5 \text{ km s}^{-1}$, $\lambda_{\text{max}} \simeq 1 \text{ pc}$ and $M_C \simeq 860 M_\odot$. This supports the idea that the gas clumps at the peak of the CMF are created by the Toomre instability. Such low-mass gas clumps are not in the CMF in model *M0.1*. The numerical resolution of 625^2 is not sufficient to resolve such low-mass gas clumps.

However, as shown in Figure 10, the time evolution of $\overline{\Sigma_{\text{gas}}}(R)$ in both models agree well with each other, indicating that the angular momentum transfer is calculated with similar accuracy in both models. These facts indicate that massive gas clumps play a central role in the angular momentum/mass transfer. Actually, the higher mass side ($\gtrsim 10^4 M_\odot$) of the CMF in both models is similar during the simulations. Therefore, the angular momentum and mass in a clumpy turbulent disk are mainly transported by a mutual interaction between massive gas clumps of $M \gtrsim 10^4 M_\odot$.

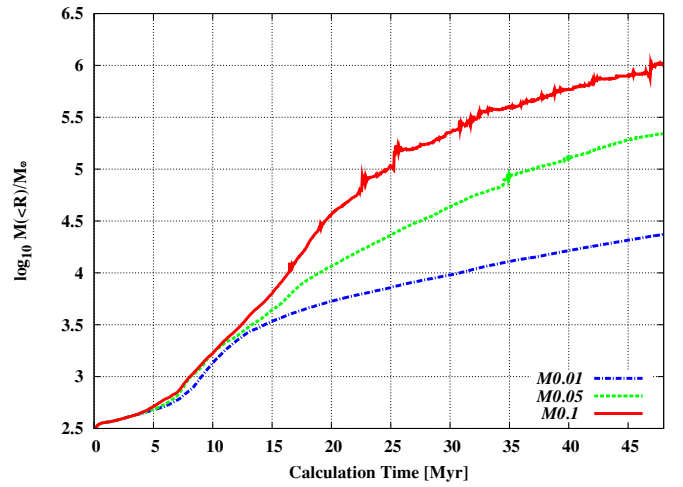


Figure 12. Time evolution of gas mass inside $R = 2.5 \text{ pc}$ in models *M0.01*, *M0.05*, and *M0.1*. Models are shown by the blue dot-dashed line (*M0.01*), the green dotted line (*M0.05*), and the red solid line (*M0.1*), respectively.

(A color version of this figure is available in the online journal.)

3.5. Relation between \dot{M}_{host} and $\dot{M}_{\text{G.C.}}$

Here, we show the relation of the gas supply rate to the galactic center $\dot{M}_{\text{G.C.}}$ and the gas supply rate from the host galaxy \dot{M}_{host} . Figure 12 shows the time evolution of the gas mass within 2.5 pc , $M_{2.5}$ for each model. $M_{2.5}$ rapidly increases in the larger \dot{M}_{host} model. There are several jumps of the gas mass in models *M0.05* and *M0.1*. These correspond to the gas supply by an infall of massive gas clumps.

We estimate the gas supply rate $\dot{M}_{\text{G.C.}}$ into $R = 2.5 \text{ pc}$ from the time variation of $M_{2.5}$ for $t = 40\text{--}48 \text{ Myr}$. In model *M0.01*, $\dot{M}_{\text{G.C.}}$ is $9.0 \times 10^{-4} M_\odot \text{yr}^{-1}$, which corresponds to 9% of \dot{M}_{host} . In model *M0.05*, $\dot{M}_{\text{G.C.}}$ is $1.35 \times 10^{-2} M_\odot \text{yr}^{-1}$, which is 27% of \dot{M}_{host} . In model *M0.1*, $\dot{M}_{\text{G.C.}}$ is $4.5 \times 10^{-2} M_\odot \text{yr}^{-1}$, which is 45% of \dot{M}_{host} . In model *M0.01*, only the outer part of the nuclear gas disk becomes self-gravitationally unstable at $t = 48 \text{ Myr}$. Since \dot{M}_{host} is small in this model, we continue the simulation of model *M0.01* to $t = 120 \text{ Myr}$ and find that $\dot{M}_{\text{G.C.}}$ increases up to $4 \times 10^{-3} M_\odot \text{yr}^{-1}$, which is 40% of \dot{M}_{host} . This is simply because the self-gravitationally unstable region extends inward with time. In model *M0.1*, $\dot{M}_{\text{G.C.}}$ increases up to 75% of \dot{M}_{host} when we continue the simulation to $t = 120 \text{ Myr}$. This is probably due to a decrease in the average Toomre Q value of the nuclear gas disk rather than the extension of the self-gravitationally unstable region, since the whole region of the nuclear gas disk is already self-gravitationally unstable at $t = 48 \text{ Myr}$. These results show that $\dot{M}_{\text{G.C.}}$ increases through the following two phases: (1) extension of the self-gravitationally unstable region toward the center; and (2) subsequent decrease of the average Toomre Q value of the nuclear gas disk.

3.6. \dot{M}_{host} and Random Motion of Gas Clumps

As we described above, the gas motion in the nuclear gas disk is turbulent. The gas supply rate to the galactic center increases with \dot{M}_{host} . It is interesting to investigate the relation between the turbulent gas motion in the nuclear gas disk and \dot{M}_{host} .

We measure the turbulent motion in the nuclear gas disk using the velocity dispersion σ_v , which is defined as

$$\sigma_v \equiv \sqrt{\frac{\sum_{i,j} \delta v_{i,j}^2 \Sigma_{\text{gas},i,j}}{\sum_{i,j} \Sigma_{\text{gas},i,j}}}, \quad (15)$$

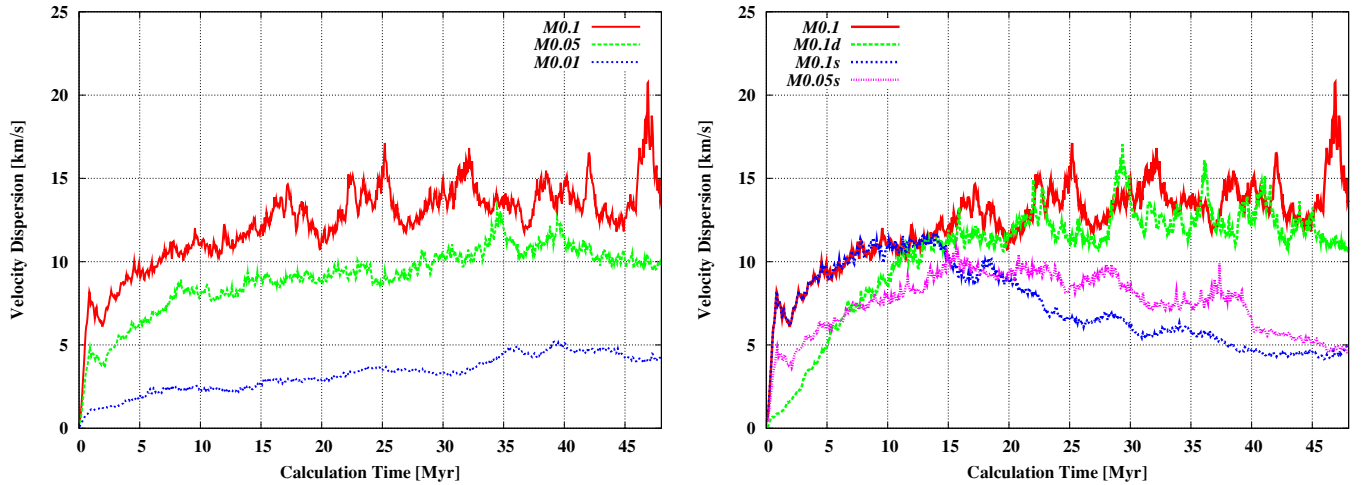


Figure 13. Time evolution of the velocity dispersions in models *M0.01*, *M0.05*, and *M0.1* (left panel) and in models *M0.1*, *M0.1d*, *M0.1s*, and *M0.05s* (right panel). (A color version of this figure is available in the online journal.)

where $\delta v_{i,j}^2 = (v_{x,i,j} - v_{x0,i,j})^2 + (v_{y,i,j} - v_{y0,i,j})^2$, $v_{x0,i,j}$ and $v_{y0,i,j}$ are the x and y components of the azimuthally averaged circular velocity at the radius $R_{i,j} = (x_i^2 + y_j^2)^{1/2}$. A similar definition is used in Shetty & Ostriker (2008) to measure the degree of the turbulent motion in the Galactic disk.

We show the time evolution of the velocity dispersion σ_v for each \dot{M}_{host} in the left panel of Figure 13. In models *M0.05* and *M0.1*, σ_v gradually increases with time and saturates with oscillations. Many peaks of σ_v correspond to coalescences of massive gas clumps or strong gravitational encounters between massive gas clumps. These processes lead to large deviation from circular motion. On the other hand, in model *M0.01*, σ_v slowly increases with no large oscillation. In this model, the mass of the nuclear gas disk is smaller than the other models, and large gas clumps are not formed. Because the interaction of small gas clumps is weak, σ_v is small. The saturated value of σ_v is larger for larger \dot{M}_{host} models. This is due to the fact that massive clumps are formed in larger \dot{M}_{host} models. We approximate our numerical results as $\sigma_v \propto \dot{M}_{\text{host}}^{1/2}$.

In order to understand the property of the nuclear gas disk, it is important to investigate the excitation mechanism of the random motion of gas clumps in the nuclear gas disk. Two excitation mechanisms are possible. One is gravitational encounters between gas clumps. Gravitational encounters lead to deviation from circular motion. When massive gas clumps undergo gravitational encounters, their deviation becomes large. We can explain the large saturated value of σ_v in larger \dot{M}_{host} models by the fact that the mean mass of gas clumps is larger in larger \dot{M}_{host} models. The release of the potential energy of the supplied gas may be the another source of the turbulent motion. The released potential energy of \dot{M}_{host} is $\Delta\Phi \sim G\dot{M}_{\text{host}}(M_{\text{tot}}(< R_{\text{out}})/R_{\text{out}} - M_{\text{tot}}(< R_{\text{src}})/R_{\text{src}})$, where R_{out} is the radius of the outer edge of the nuclear gas disk, R_{src} is the radius of the sources, and $M_{\text{tot}}(< R)$ is the total mass within R .

In order to check the excitation mechanism of the turbulence in the nuclear gas disk, we perform additional numerical simulations. We first simulate models with time-dependent \dot{M}_{host} , models *M0.05s* and *M0.1s*, in which \dot{M}_{host} is initially constant and then stops as shown in Table 1. We show the time evolution of the velocity dispersion σ_v of these models in the right panel of Figure 13. After \dot{M}_{host} stops, the velocity

dispersion decreases with time. The number of gas clumps also decreases with time. This is due to the decrease in self-gravitationally unstable regions in the nuclear gas disk by the inward mass transfer. This result suggests that gravitational encounters play an important role in the excitation of turbulence in the nuclear gas disk. Next, we perform a numerical simulation assuming $R_{\text{src}} = R_{\text{out}}$ and therefore $\Delta\Phi = 0$ (model *M0.1d*). The time evolution of the velocity dispersions in models *M0.1* and *M0.1d* is shown in the right panel of Figure 13. This figure shows that the velocity dispersions of both models are almost the same. This indicates that a large fraction of the released potential energy of the supplied gas dissipates in model *M0.1*. The small difference between them may be due to a small contribution of the potential energy of the supplied gas. Therefore, we conclude that the turbulent motion in the nuclear gas disk is mainly excited by the gravitational encounters between gas clumps. The contribution of the release of the potential energy of the supplied gas to the turbulent motion is small.

3.7. The Massive M_{SMBH} Case

Because it is very interesting to investigate the massive central SMBH case, we perform a numerical simulation for M_{SMBH} of $10^8 M_{\odot}$. In the outer part of the nuclear gas disk, gas clumps are formed by self-gravitational instability. Some of the gas clumps lose their angular momentum via gravitational interactions and migrate inward. In the inner part of the nuclear gas disk, most of the gas clumps are disrupted by the strong tidal force of the SMBH. As a result, a massive gas ring is formed in the radii of 2–8 pc. In this gas ring, a one-armed gas spiral is formed. To show the formation mechanism of the one-armed gas spiral, we perform a Fourier mode analysis of the gas ring, as in Wada & Norman (2001). We also calculate the global Toomre Q parameter, which we define as a mass-weighted average of the local Toomre Q parameter in the gas ring. We show the time evolution of the Fourier mode amplitudes and the global Toomre Q parameter in Figures 14 and 15, respectively. Figure 14 shows that the $m = 1$ mode dominates after $t > 25$ Myr. After $t > 25$ Myr, the global Toomre Q parameter becomes lower than unity, as shown in Figure 15. This suggests that the one-armed gas spiral is excited by self-gravitational instability and a one-armed gas spiral can be excited in the

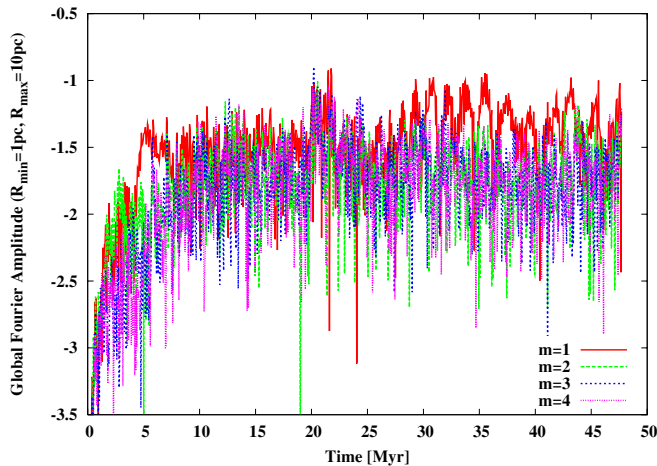


Figure 14. Time evolution of the amplitude of global Fourier modes.
(A color version of this figure is available in the online journal.)

region dominated by the Kepler potential of the SMBH. We show the time evolution of the gas spiral in Figure 16. The rotational period of the one-armed gas spiral is less than a few Myr. The one-armed gas spiral may be important for further gas supply to the galactic center. To investigate this possibility, simulations with higher resolution are needed.

The one-armed gas spiral may be a candidate for an H₂O mega-maser emission site (Maoz & McKee 1998), since H₂O mega-maser is emitted from high density gas. Almost all H₂O mega-maser sources are observed at the subparsec distance from galactic centers. In our simulation, we show that the one-armed gas spiral is formed near the outer radius of the SMBH-dominated region. For a less massive SMBH, a one-armed gas spiral is expected to be formed at smaller radii.

4. DISCUSSIONS

4.1. Gas Supply Process to the Galactic Center

In this paper, we perform hydrodynamical simulations of the nuclear gas disk, assuming gas supply from the host galaxy, in order to investigate the gas supply process from the nuclear gas disk to the Galactic center. The mass of the nuclear gas disk increases gradually with time by the gas supply from the host galaxy, and its outer part becomes self-gravitationally unstable. In the outer part, small gas clumps form by self-gravitational instability. These gas clumps coalesce into more massive gas clumps. In models *M0.05* and *M0.1*, such coalescences occur repeatedly and very massive gas clumps form, since small gas clumps form more actively in these models than in model *M0.01*. The gas clumps interact gravitationally with each other and exchange their angular momentum. The gas clumps that lose their angular momentum migrate inward. On the other hand, the gas clumps that gain angular momentum are scattered to outer radii. Thus, the mass and the angular momentum are transferred by the gas clumps. In model *M0.1*, very massive gas clumps form near the Galactic center ($R \lesssim 10$ pc). Some of those that lose their angular momentum via gravitational encounter migrate directly to the center without being destroyed by the strong tidal force. This process occurs a few times during the simulation. These results indicate that the starbursts should occur in the nuclear gas disk.

In order to investigate the effect of the numerical resolution, we compare the different numerical resolution models (625²

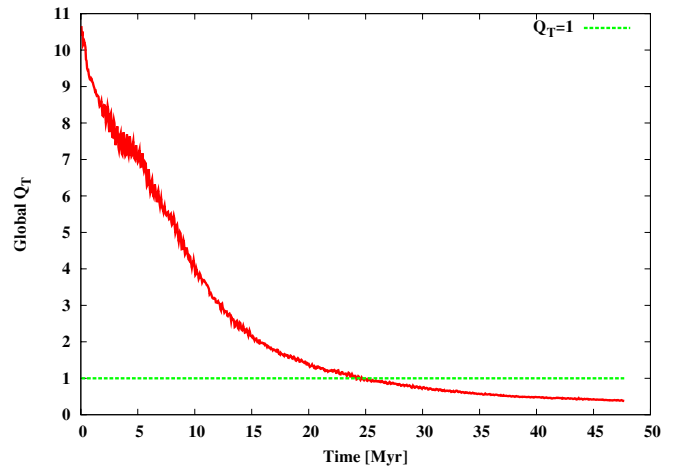


Figure 15. Time evolution of the global Toomre parameter.
(A color version of this figure is available in the online journal.)

and 1215²). The time evolution of the radial mass profiles in both models agree well with each other. On the other hand, the CMFs of both models do not agree with each other except on the high-mass side. From these results, we conclude that more massive gas clumps play a more important role in the mass and angular momentum transfer in the nuclear gas disk.

We show the importance of gravitational interactions between gas clumps in the gas supply process in the nuclear gas disk. The role of gravitational interactions between giant molecular clouds (GMCs) in the galactic disk have already been investigated analytically and numerically by several authors (Fukunaga 1983, 1984; Tosa & Fukunaga 1986; Jog & Ostriker 1988; Fukunaga & Tosa 1989a, 1989b; Gammie et al. 1991). Using *N*-body simulations and assuming inelastic collisions between GMCs, Fukunaga & Tosa (1989b) show that gravitational interactions between GMCs act as kinematics viscosity and trigger a radial inflow of GMCs. Fukunaga (1984), Tosa & Fukunaga (1986), and Fukunaga & Tosa (1989a) show that the observed value of the velocity dispersion of the GMCs in our Galaxy is well explained by mutual gravitational interactions. In their simulations, they do not consider a cloud mass spectrum. Therefore, the role of the cloud mass spectrum in radial inflow is not clear. Furthermore, they introduce an artificial friction force to model inelastic collisions of the GMCs. In our simulation, the cloud mass spectrum is naturally taken into account because of full hydrodynamic simulation, and the uncertainty of the frictional force is fully excluded.

In this study, we focus on hydrodynamic effects and do not take into account other important processes, such as star formation and stellar feedbacks. Here, we discuss star formation processes in the massive gas clumps, the effects of the star formation, and stellar feedback processes. We compare the surface density of the massive clumps with starburst galaxies to discuss high-mass star formation. The mean surface densities of the nuclear gas disks given in Sections 3.1–3.3 attain roughly $400 M_{\odot} \text{ pc}^{-2}$ in model *M0.01*, $1000 M_{\odot} \text{ pc}^{-2}$ in model *M0.05*, and $2000 M_{\odot} \text{ pc}^{-2}$ in model *M0.1*. These surface densities are as high as those observed in starburst galaxies (Kennicutt 1998; Bigiel et al. 2008), and we expect high-mass star formation in the nuclear gas disk if the initial mass function is the Salpeter function. However, the star formation process in the nuclear gas disk may be very different from that in starburst galaxies, since tidal force is very strong in the Galactic center. A detailed

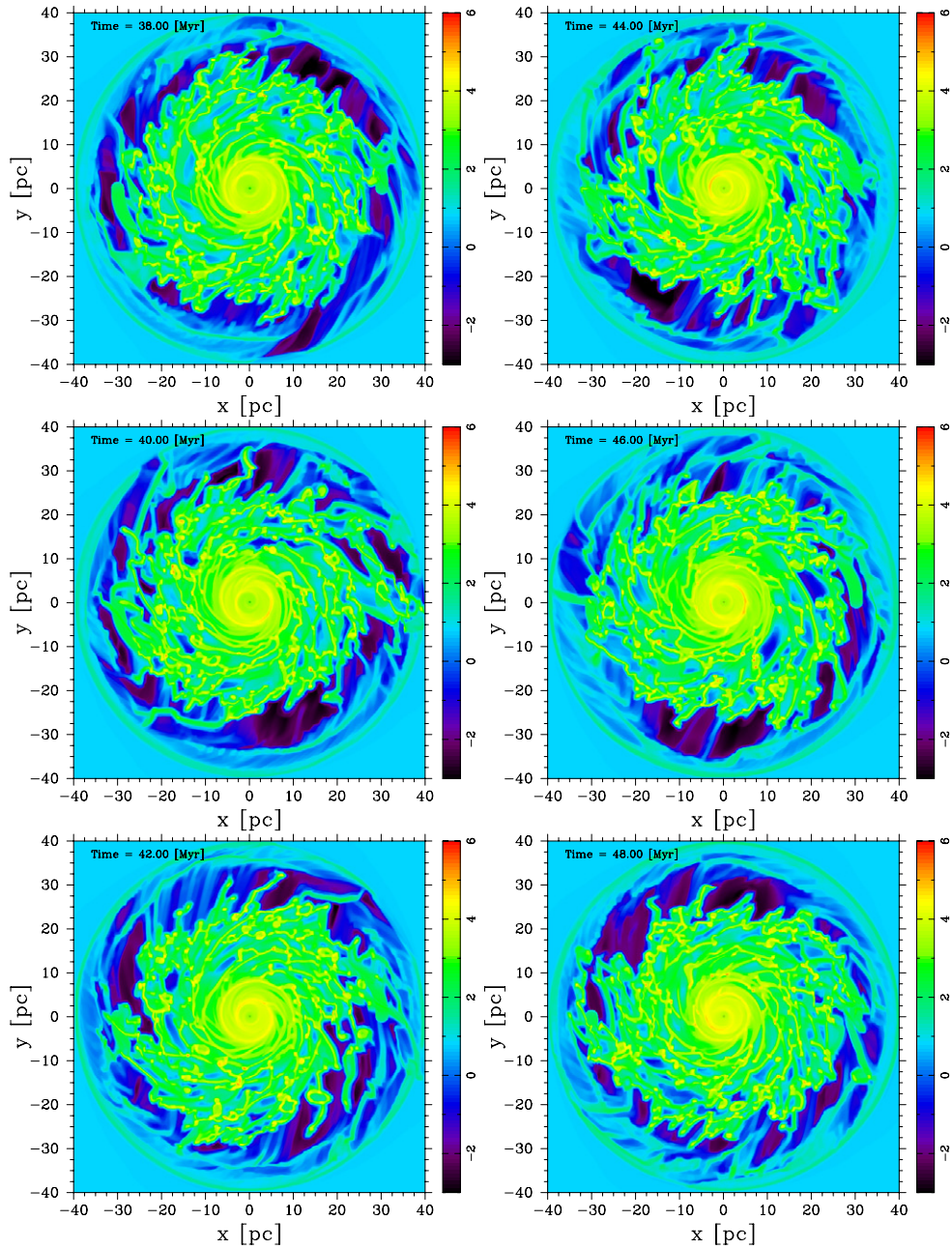


Figure 16. Time evolution of model *M0.1CMC8* during last 10 Myr. The figures in the upper left corners of each panel and the colors are the same as in Figure 3. (A color version of this figure is available in the online journal.)

study is needed to explore high-mass star formation in the nuclear gas disk. We note a possible process of compact star cluster formation in the nuclear gas disk. In the outer part of the nuclear gas disk ($R > 15$ pc), some of the massive gas clumps collide with each other with a large relative velocity of several 10 km s^{-1} . Due to such high-speed clump–clump collision, very compact star clusters like the Arches cluster and the Quintuplet cluster may be formed far from the Galactic center (Stole et al. 2008, 2009). It is interesting to study such a possibility. The gas supply process by the massive gas clump migration must be affected by star formation if the star formation timescale is shorter than the migration timescale of the gas clumps, since massive gas clumps are important in the mass and angular momentum transfer process in the nuclear gas disk. The typical migration timescale of massive gas clumps

near the Galactic center ($R \lesssim 10$ pc) is about 1 Myr. The star formation timescale of the gas clumps is estimated to be $C t_{\text{ff}}$, where C is a proportional constant and t_{ff} is the free-fall time of the gas clump (Krumholz & McKee 2005; Krumholz & Tan 2007). For the typical values, the star formation timescale is $1.65(C/30)(R/0.5 \text{ pc})^3 (M_{\text{clump}}/10^4 M_{\odot})^{-1} \text{ Myr}$ (Krumholz & Tan 2007). The star formation timescale is comparable to the migration timescale. Thus, it is necessary to study how star formation affects the process of gas supply to the Galactic center. Stellar feedback processes such as supernovae, stellar winds, and FUV radiation from massive stars, are also important because these processes affect the self-gravitational stability of the nuclear gas disk through the heating and the excitation of the turbulent motion of the gas in the nuclear gas disk. In the context of active galactic nucleus starburst torus, Wada (2002)

and Wada et al. (2009) showed the important role of turbulent viscosity driven by a supernova in gas inflow to the center. Thus, it is interesting to take these processes into account. The effects of star formation and stellar feedback processes will be investigated in subsequent papers.

4.2. Formation of the CND

Formation of the CND may be related to the formation of young massive stars in the Galactic center. We have shown that the massive gas clumps with low angular momentum are formed in the nuclear gas disk and the central mini disk of <5 pc around the Galactic center can be formed by the migration of the massive gas clumps discussed in this paper. The migration time is less than 1 Myr, and the mass of massive gas clumps is in the range of $M = 10^4$ – $10^5 M_\odot$. The mass of the central mini disk is more than $3 \times 10^5 M_\odot$ after the first migration of the massive gas clump to the Galactic center. The mass and size agree well with the CND (Shukla et al. 2004; Christopher et al. 2005; Montero-Castaño et al. 2009). Šubr et al. (2009) argued that the young stellar disks at the Galactic center are destroyed by the gravitational torque in the timescale of 6 Myr if the mass of the CND exceeds $0.3 M_{\text{SMBH}}$. The mass of the central mini disk mentioned above is less than this value. Therefore, our results are consistent with the stable young stellar disks. Thus, we can explain the formation of the CND by the migration of low angular momentum gas clouds found in our numerical results.

In connection with the formation of the CND, capture of a very low angular momentum cloud in the Galactic center has already been discussed (Sanders 1998; Bonnell & Rice 2008; Mapelli et al. 2008; Hobbs & Nayakshin 2009). Such low angular momentum clouds can be produced by dynamic friction against the bulge stars if molecular clouds with more than $10^6 M_\odot$ are formed in the CMZ (Stark et al. 1991). However, the mass of molecular clouds is too high to explain the formation of the CND (Shukla et al. 2004; Christopher et al. 2005; Montero-Castaño et al. 2009). The mass of the migrating gas clumps in our results is much smaller than such high-mass molecular clouds. Our numerical results give an explanation for the origin of the low angular momentum clouds. There are other ways in which the CND can be produced (see Genzel et al. 2010). For example, partial capture of the molecular gas cloud radially moving toward the Galactic center has been discussed (Wardle & Yusef-Zadeh 2008).

Migration of massive gas clumps is related to the in situ formation scenario, which is proposed to resolve the paradox of youth, that is, the discrepancy between the short age of young stars in the Central cluster and the long migration time of a young star cluster formed in the outside of the Galactic center, assuming the young star cluster forms the Central cluster after its migration to the Galactic center (Morris 1993; Genzel et al. 1996; Ghez et al. 2003; Levin & Beloborodov 2003; Nayakshin et al. 2007; Bonnell & Rice 2008; Hobbs & Nayakshin 2009). In the in situ formation scenario, low angular momentum gas clouds captured by the SMBH form a gas disk around the SMBH via a strong tidal force, and the gas disk rapidly fragments by gravitational instability and forms young stars. Several numerical studies have been conducted to investigate this process and have shown that the Central cluster can be explained by this scenario (Nayakshin et al. 2007; Bonnell & Rice 2008; Hobbs & Nayakshin 2009). More detailed discussion of the origin of young stars is found in the review paper by Genzel et al. (2010).

It is interesting to predict evidence of clump migrations due to gravitational encounters in the nuclear gas disk as found in this paper. We calculate the line-of-sight velocities of gas clumps near the Galactic longitude $l = 0$ to find evidence of the non-circular motion of gas clumps excited by strong gravitational encounters in our results. Abrupt changes in the non-circular motions are clear evidence of migration motion excited by strong gravitational encounters. The maximum change of non-circular velocity near $l = 0$ is roughly 40 km s^{-1} by this process. If we detect such a change in non-circular motion of massive gas clumps, it will be strong evidence of clump migrations excited by strong gravitational encounters.

4.3. Size–Velocity–Width Relation

Comparison of the statistical properties of the gas clumps in the nuclear gas disk with those of the CMZ and the Galactic disk may help us understand the formation and the evolution of molecular clouds in different regions of the Galaxy. Here, we focus on the size–velocity–width relation, which is one of the empirical relations observed in the Galactic disk and the CMZ. This relation is first obtained from the observations of the GMCs in the Galactic disk. It is the relation between the sizes S and the velocity widths σ of the GMCs that is described as $\sigma \propto S^{0.5}$ (Dame et al. 1986; Scoville et al. 1987; Solomon et al. 1987). Oka et al. (2001) have shown that such a relation holds for the molecular clouds in the CMZ. For comparison with these observations, we give the size and internal velocity dispersion of the gas clumps in models *M0.1* and *M0.1hr* in Figures 17 and 18, respectively. Interestingly, the distribution of the internal velocity dispersion in the nuclear gas disk is similar to that in the CMZ (Oka et al. 2001). We show the S and σ values for models *M0.1* and *M0.1hr* in Figure 19. The black dashed line in this figure is the best-fit line obtained by the method of least squares for these values. The best-fit formula is

$$\sigma = 11.03_{-0.318}^{+0.323} S^{0.569 \pm 0.023} \text{ km s}^{-1}, \quad (16)$$

where S is in parsecs. This relation agrees with $\sigma^2 \sim G\pi S^2 \bar{\Sigma}_{\text{cl}}/S \propto S$ for constant $\bar{\Sigma}_{\text{cl}}$, which is the mean surface density of clumps. The exponent of S in Equation (16) agrees well with the exponents in the CMZ (Oka et al. 2001) and the Galactic disk (Dame et al. 1986; Scoville et al. 1987; Solomon et al. 1987). This agreement suggests that the physical process that determines the velocity dispersion of the gas clouds is similar in these regions. The coefficient in Equation (16) for the S – σ relation of the clumps in the nuclear gas disk is larger than those in the CMZ ($\approx 4 \text{ km s}^{-1}$) and in the Galactic disk ($\lesssim 1 \text{ km s}^{-1}$; see the references cited above). These coefficients are scaled as $\bar{\Sigma}^{0.5}$, where $\bar{\Sigma}$ is the mean gas surface density in each region, since the average surface density of model *M0.1* is $2000 M_\odot \text{ pc}^{-2}$ and the average surface densities of the CMZ and the Galactic disk are $400 M_\odot \text{ pc}^{-2}$ and $20 M_\odot \text{ pc}^{-2}$, respectively. This scaling can be explained if the average surface densities of clumps are proportional to the critical surface density, which is determined by the Toomre instability as shown in the previous sections.

5. SUMMARY

We summarize our study as follows:

1. To investigate the gas supply process in the Galactic center, we perform numerical simulations of the nuclear gas disk, assuming gas supply from the host galaxy. During the early

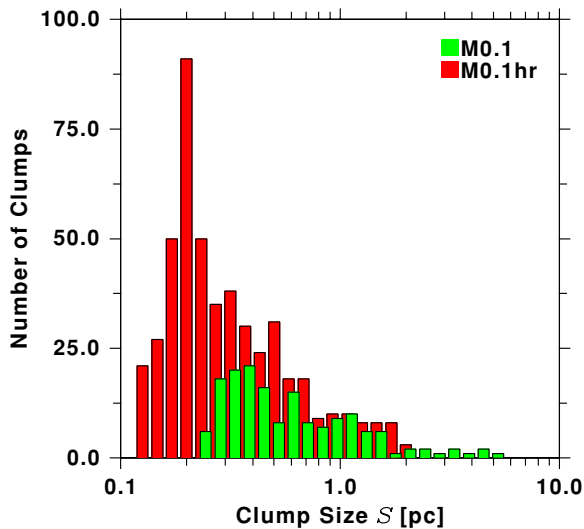


Figure 17. Number distribution of the clump size in models *M0.1* and *M0.1hr* at $t = 27.5$ Myr. We slightly offset the columns of model *M0.1* rightward.
(A color version of this figure is available in the online journal.)

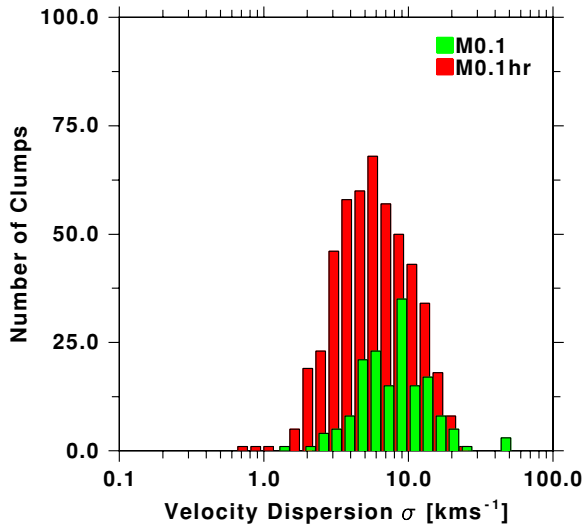


Figure 18. Number distribution of the internal velocity dispersion of the gas clumps in models *M0.1* and *M0.1hr* at $t = 27.5$ Myr. We slightly offset the columns of model *M0.1* rightward.
(A color version of this figure is available in the online journal.)

stage of the simulation, the outer part of the nuclear gas disk becomes self-gravitationally unstable due to the supplied gas from the host galaxy. As the mass of the nuclear gas disk increases, many gas clumps are formed by self-gravitational instability. These gas clumps coalesce into massive gas clumps. The massive gas clumps exchange their angular momentum via gravitational interactions. Massive gas clumps that lose their angular momentum migrate inward. The gas supply to the Galactic center is realized by the migration of massive gas clumps. Its rate attains about half that of the gas supply from the host galaxy, when the whole region of the nuclear gas disk becomes self-gravitationally unstable. The comparison of results of simulations with different resolutions indicates that gravitational encounters of massive gas clumps play an important role in the angular momentum transfer in the nuclear gas disk.

2. From numerical simulations for different gas supply rates from the host galaxy, we show that the turbulent velocity in

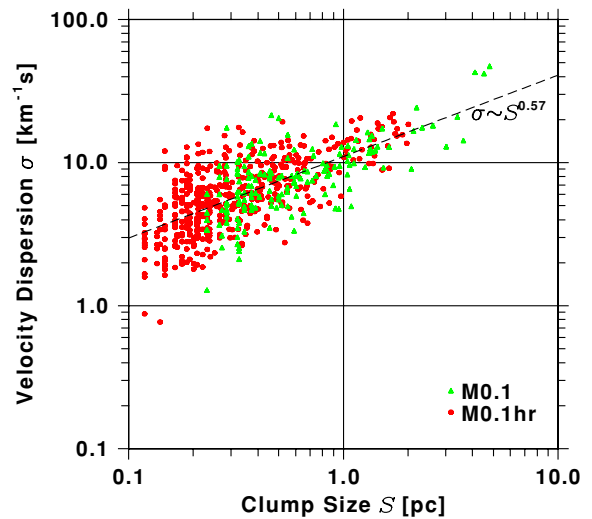


Figure 19. S – σ plot for models *M0.1* and *M0.1hr* at $t = 27.5$ Myr.
(A color version of this figure is available in the online journal.)

the nuclear gas disk is larger in larger \dot{M}_{host} models and is nearly constant with time. The turbulent velocity is likely to be maintained by gravitational encounters between massive gas clumps. We show the empirical relation $\sigma_v \propto \dot{M}_{\text{host}}^{1/2}$ from our results. Mass of clumps formed in the nuclear gas disk increases with \dot{M}_{host} .

3. To show the effect of the central SMBH, we perform a numerical simulation with M_{SMBH} of $10^8 M_{\odot}$. The evolution of the outer part of the nuclear gas disk is similar to that of the model with M_{SMBH} of $3 \times 10^6 M_{\odot}$. Near the massive SMBH, gas clumps are rapidly destroyed by the extremely strong tidal force of the massive SMBH. Consequently, the gas supply to the galactic center by migration of massive gas clumps is limited to outside the strong tidal force region. As a result, a massive gas ring is formed at the radius of 2–8 pc. In this gas ring, a one-armed gas spiral is formed by self-gravitational instability. This gas spiral may be a candidate for a mega-maser disk model and may play an important role in the evolution of the gas ring. Further study is needed to examine this interesting possibility.

We thank the anonymous referee for helpful suggestions that improved the paper. We thank Professor Masayuki Fujimoto for continuous encouragement. D.N. is supported by CPS running under the auspices of the MEXT Global GCOE Program entitled “Foundation of International Center for Planetary Science.” The numerical simulations were carried out on Cray XT4 at Center for Computational Astrophysics, CfCA, of National Astronomical Observatory of Japan (NAOJ). The page charge of this paper is supported by the NAOJ.

APPENDIX A

M-AUSMPW⁺

In this appendix, we first explain the discretization of the hydrodynamic Equations (1)–(3) and then give the formula of the M-AUSMPW⁺. In Cartesian coordinates, the two-dimensional hydrodynamic equation can be written as

$$\frac{\partial \mathbf{Q}}{\partial t} + \frac{\partial \mathbf{F}}{\partial x} + \frac{\partial \mathbf{G}}{\partial y} = \mathbf{S}. \quad (\text{A1})$$

The conserved variable vector \mathbf{Q} , the flux vector \mathbf{F} , \mathbf{G} , and the vector of the source terms \mathbf{S} are given by

$$\mathbf{Q} = \begin{pmatrix} \rho \\ \rho u \\ \rho v \\ \rho E \end{pmatrix}, \quad \mathbf{F} = \begin{pmatrix} \rho u \\ \rho u^2 + p \\ \rho uv \\ \rho u H \end{pmatrix},$$

$$\mathbf{G} = \begin{pmatrix} \rho v \\ \rho uv \\ \rho v^2 + p \\ \rho v H \end{pmatrix}, \quad (\text{A2})$$

$$\mathbf{S} = \mathbf{S}_{\text{grav}} + \mathbf{S}_{\text{rad}} + \mathbf{S}_{\text{src}}$$

$$= \begin{pmatrix} 0 \\ \rho g_x \\ \rho g_y \\ \rho \mathbf{v} \cdot \mathbf{g} \end{pmatrix} + \begin{pmatrix} 0 \\ 0 \\ 0 \\ \Gamma - \Lambda \end{pmatrix} + \begin{pmatrix} (d/dt)\rho_s \\ (d/dt)(\rho_s u_s) \\ (d/dt)(\rho_s v_s) \\ (d/dt)(\rho_s E_s) \end{pmatrix}, \quad (\text{A3})$$

where ρ is the density, $\mathbf{v} = (u, v)^T$ is the velocity, p is the pressure, E is the sum of the specific internal energy and the specific kinematic energy, H is the sum of the specific enthalpy and the specific kinematic energy, $\mathbf{g} = (g_x, g_y)^T$ is the gravity, and the quantities indicated by a subscript of “s” are source terms. These quantities are given by the following equations:

$$E = e + \frac{1}{2}(u^2 + v^2), \quad (\text{A4})$$

$$p = (\gamma - 1)\rho e, \quad (\text{A5})$$

$$H = E + \frac{p}{\rho}, \quad (\text{A6})$$

where e is the specific internal energy.

With the discrete representation $t^n = t^0 + n\Delta t$, $x_i = x_0 + i\Delta x$, and $y_j = y_0 + j\Delta y$, Equation (A1) can be discretized as

$$\mathbf{Q}_{i,j}^{n+1} = \mathbf{Q}_{i,j}^n - \Delta t \left[\frac{\mathbf{F}_{i+\frac{1}{2},j}^n - \mathbf{F}_{i-\frac{1}{2},j}^n}{\Delta x} + \frac{\mathbf{G}_{i,j+\frac{1}{2}}^n - \mathbf{G}_{i,j-\frac{1}{2}}^n}{\Delta y} \right] + \Delta t \mathbf{S}_{i,j}, \quad (\text{A7})$$

where vectors in the form of $\mathbf{a}_{i,j}^n$ show some approximation of $\mathbf{a}(t^n, x_i, y_j)$. In the finite volume method, $\mathbf{Q}_{i,j}^n$ is considered as the spatial-averaged value, that is,

$$\mathbf{Q}_{i,j}^n \equiv \frac{1}{\Delta x \Delta y} \int_{x_{i-\frac{1}{2}}}^{x_{i+\frac{1}{2}}} \int_{y_{j-\frac{1}{2}}}^{y_{j+\frac{1}{2}}} \mathbf{Q}(t^n, x, y) dx dy. \quad (\text{A8})$$

$\mathbf{F}_{i\pm\frac{1}{2},j}^n$ and $\mathbf{G}_{i,j\pm\frac{1}{2}}^n$ are called the numerical fluxes. The subscript $i + \frac{1}{2}$ indicates the cell interface between (i, j) and $(i + 1, j)$. The same rule holds for the other subscripts that contain $\frac{1}{2}$. Therefore, the problem comes down to how we evaluate the numerical fluxes at the cell interfaces. In this study, we use the M-AUSMPW⁺ to evaluate the numerical fluxes.

The numerical flux of the M-AUSMPW⁺ (Kim & Kim 2005b) is written as

$$\mathbf{F}_{i+\frac{1}{2}} = a_{i+\frac{1}{2}} (\tilde{\mathcal{M}}_L^+ \Phi_{L,\frac{1}{2}} + \tilde{\mathcal{M}}_R^- \Phi_{R,\frac{1}{2}}) + (\mathcal{P}^+(M_L) \mathbf{P}_L + \mathcal{P}^-(M_R) \mathbf{P}_R) \quad (\text{A9})$$

$$\Phi_{\frac{1}{2}} = (\rho_{\frac{1}{2}}, \rho_{\frac{1}{2}} u_{\frac{1}{2}}, \rho_{\frac{1}{2}} v_{\frac{1}{2}}, \rho_{\frac{1}{2}} H_{\frac{1}{2}}), \quad (\text{A10})$$

where $H_{L,R,\frac{1}{2}} = \frac{\gamma}{\gamma-1} \frac{p_{L,R,\frac{1}{2}}}{\rho_{L,R,\frac{1}{2}}} + \frac{1}{2}(u_{L,R,\frac{1}{2}}^2 + v_{L,R,\frac{1}{2}}^2)$ and $a_{i+\frac{1}{2}}$ shows the sound speed at the cell interface. $a_{i+\frac{1}{2}}$ is defined as

$$a_{i+\frac{1}{2}} = \begin{cases} \frac{a_s^2}{\max(|U_L|, a_s)}, & \frac{1}{2}(U_L + U_R) > 0, \\ \frac{a_s^2}{\max(|U_R|, a_s)}, & \frac{1}{2}(U_L + U_R) \leq 0, \end{cases} \quad (\text{A11})$$

$$a_s = \sqrt{\frac{2(\gamma-1)}{\gamma+1} H_{\text{normal}}}, \quad (\text{A12})$$

$$H_{\text{normal}} = \frac{1}{2} \left(H_L - \frac{1}{2} V_L^2 + H_R - \frac{1}{2} V_R^2 \right), \quad (\text{A13})$$

where $U_{L,R}$ is the velocity component normal to a cell interface and $V_{L,R}$ is the velocity component parallel to a cell interface.

The advected quantities $\Phi_{L,R,\frac{1}{2}}$ are

$$\Phi_{L,\frac{1}{2}} = \Phi_L + \frac{\max[0, (\Phi_R - \Phi_L)(\Phi_{L,\text{superbee}} - \Phi_L)]}{(\Phi_R - \Phi_L)|\Phi_{L,\text{superbee}} - \Phi_L|} \min \left[a \frac{|\Phi_R - \Phi_L|}{2}, |\Phi_{L,\text{superbee}} - \Phi_L| \right] \quad (\text{A14})$$

$$\Phi_{R,\frac{1}{2}} = \Phi_R + \frac{\max[0, (\Phi_L - \Phi_R)(\Phi_{R,\text{superbee}} - \Phi_R)]}{(\Phi_L - \Phi_R)|\Phi_{R,\text{superbee}} - \Phi_R|} \min \left[a \frac{|\Phi_L - \Phi_R|}{2}, |\Phi_{R,\text{superbee}} - \Phi_R| \right], \quad (\text{A15})$$

where $a = 1 - \min(1, \max(|M_L|, |M_R|))^2$ and $\Phi_{L,R,\text{superbee}}$ show the interpolated values of Φ at a cell interface using the superbee flux limiter. The Mach numbers of the left and right cells are defined as

$$M_{L,R} = \frac{U_{L,R}}{a_{i+\frac{1}{2}}}. \quad (\text{A16})$$

We evaluate $\Phi_{L,R}$ using the MLP5.

$\tilde{\mathcal{M}}_L^+$ and $\tilde{\mathcal{M}}_R^-$ are defined as

1. for $m_{i+\frac{1}{2}} \geq 0$,

$$\tilde{\mathcal{M}}_L^+ = \mathcal{M}^+(M_L) + \mathcal{M}^-(M_R)[(1-w)(1+f_R) - f_L] \quad (\text{A17})$$

$$\tilde{\mathcal{M}}_R^- = \mathcal{M}^-(M_R)w(1+f_R) \quad (\text{A18})$$

2. for $m_{i+\frac{1}{2}} < 0$,

$$\tilde{\mathcal{M}}_L^+ = \mathcal{M}^+(M_L)w(1+f_L) \quad (\text{A19})$$

$$\tilde{\mathcal{M}}_R^- = \mathcal{M}^-(M_R) + \mathcal{M}^+(M_L)[(1-w)(1+f_L) - f_R], \quad (\text{A20})$$

where $m_{i+\frac{1}{2}}$ represents the Mach number at a cell interface and is defined as $m_{i+\frac{1}{2}} = \mathcal{M}^+(M_L) + \mathcal{M}^-(M_R)$.

The weight functions w and $f_{L,R}$ are defined as

$$w = \max[w_1, w_2], \quad (\text{A21})$$

$$w_1 = 1 - \min \left(\frac{p_L}{p_R}, \frac{p_R}{p_L} \right)^3, \quad (\text{A22})$$

$$w_2 = \begin{cases} \left[1 - \min \left(1, \frac{\bar{p}_{i+1,j} - \bar{p}_{i,j}}{0.25(\bar{p}_{i+1,j+1} + \bar{p}_{i,j+1} - \bar{p}_{i+1,j-1} - \bar{p}_{i,j-1})} \right) \right]^2 \\ \quad \times \left[1 - \min \left(\frac{\bar{p}_{i,j}}{\bar{p}_{i+1,j}}, \frac{\bar{p}_{i+1,j}}{\bar{p}_{i,j}} \right) \right]^2, & i\text{-direction}, \\ \left[1 - \min \left(1, \frac{\bar{p}_{oi,j+1} - \bar{p}_{i,j}}{0.25(\bar{p}_{i+1,j+1} + \bar{p}_{i+1,j} - \bar{p}_{i-1,j+1} - \bar{p}_{i-1,j})} \right) \right]^2 \\ \quad \times \left[1 - \min \left(\frac{\bar{p}_{i,j}}{\bar{p}_{i,j+1}}, \frac{\bar{p}_{i,j+1}}{\bar{p}_{i,j}} \right) \right]^2, & j\text{-direction}, \end{cases} \quad (\text{A23})$$

$$f_{L,R} = \begin{cases} \left(\frac{p_{L,R}}{p_{i+\frac{1}{2}}} - 1 \right) (1 - w_2), & p_{i+\frac{1}{2}} \neq 0, \\ 0, & \text{otherwise}, \end{cases} \quad (\text{A24})$$

where $p_{i+\frac{1}{2}} = p_L \mathcal{P}^+(M_L) + p_R \mathcal{P}^-(M_R)$. The weight function w_1 becomes large if the pressure contrast at a cell interface is large. The weight function w_2 takes into consideration the pressure distribution around a cell interface to suppress numerical instabilities. In the i direction, w_2 becomes large if the ratio of i -directional gradient to j -directional gradient at a cell interface is small and the ratio of the pressures on both sides of the cell interface is large.

The split Mach number $\mathcal{M}^\pm(M)$ and the split pressure $\mathcal{P}^\pm(M)$ are written as follows:

$$\mathcal{M}^\pm(M) = \begin{cases} \frac{1}{2}(M \pm |M|), & |M| \geq 1, \\ \pm \frac{1}{4}(M \pm 1)^2, & |M| < 1. \end{cases} \quad (\text{A25})$$

$$\mathcal{P}^\pm(M) = \begin{cases} \frac{1}{2}(1 \pm \text{sign}(M)), & |M| \geq 1, \\ \frac{1}{4}(M \pm 1)^2(2 \mp M) \pm \alpha M(M^2 - 1)^2, & |M| < 1, \end{cases} \quad (\text{A26})$$

where $0 \leq \alpha \leq \frac{3}{16}$. In this study, we adopt $\alpha = 0$ according to the author's recommendation.

APPENDIX B

MLP

The multi-dimensional limiting process (MLP) was proposed by Kim & Kim (2005a) in order to enhance spatial accuracy and robustness in a multi-dimensional flow. The MLP is an extension of the monotone upstream-centered schemes for conservation laws (MUSCL) procedures to the multi-dimension and is based on the concept of the TVD. In the MLP, the TVD condition is applied to physical quantities at cell vertex points as well as at cell interfaces. This allows us to treat oblique shocks precisely and enhance robustness in the multi-dimensional flows. In this study, we use the MLP5, which is a fifth-order polynomial interpolation with the MLP, to evaluate $\Phi_{L,R}$. Here, we describe the two-dimensional version of the MLP interpolation formula (Yoon et al. 2008 propose the formula in the three dimension).

The MLP interpolation in the two dimension is written as

$$\Phi_L = \Phi_{i,j} + \frac{1}{2} \max(0, \min(\alpha_L \hat{r}_i, \alpha_L, \beta_L)) \Delta \Phi_{i-\frac{1}{2},j}, \quad (\text{B1})$$

$$\Phi_R = \Phi_{i+1,j} - \frac{1}{2} \max(0, \min(\alpha_R r_{i+1}, \alpha_R, \beta_R)) \Delta \Phi_{i+\frac{3}{2},j}, \quad (\text{B2})$$

for the i -direction, where $\Delta \Phi_{i+\frac{1}{2},j} \equiv \Phi_{i+1,j} - \Phi_{i,j}$ and $r_i \equiv \frac{\Delta \Phi_{i-\frac{1}{2},j}}{\Delta \Phi_{i+\frac{1}{2},j}} = \hat{r}_i^{-1}$. We omit the formula for the j -direction.

$\alpha_{L,R}$ are defined as follows: along the i -direction,

$$\alpha_L = g \left[\frac{2 \max(1, \hat{r}_i)(1 + \max(0, \hat{r}_{i+1} \tan \theta_{i+1}))}{1 + \tan \theta_i} \right],$$

$$\alpha_R = g \left[\frac{2 \max(1, r_{i+1})(1 + \max(0, r_i \tan \theta_i))}{1 + \tan \theta_{i+1}} \right]. \quad (\text{B3})$$

Along the j -direction,

$$\alpha_L = g \left[\frac{2 \max(1, \hat{r}_j)(1 + \max(0, \hat{r}_{j+1} \tan \theta_{j+1}))}{1 + \tan \theta_j} \right],$$

$$\alpha_R = g \left[\frac{2 \max(1, r_{j+1})(1 + \max(0, r_j \tan \theta_j))}{1 + \tan \theta_{j+1}} \right], \quad (\text{B4})$$

where $g(x) = \max(1, \min(2, x))$ and

$$\tan \theta_i = \left| \frac{\Phi_{i,j+1} - \Phi_{i,j-1}}{\Phi_{i+1,j} - \Phi_{i-1,j}} \right|, \quad \tan \theta_j = \left| \frac{\Phi_{i+1,j} - \Phi_{i-1,j}}{\Phi_{i,j+1} - \Phi_{i,j-1}} \right|. \quad (\text{B5})$$

The definition of $\beta_{L,R}$ depends on the order of the interpolation polynomial. Under combination with the third-order polynomial (MLP3), $\beta_{L,R}$ are defined as

$$\beta_L = \frac{1 + 2\hat{r}_i}{3}, \quad \beta_R = \frac{1 + 2r_{i+1}}{3}. \quad (\text{B6})$$

Under combination with the fifth-order polynomial (MLP5), $\beta_{L,R}$ are defined as

$$\beta_L = \frac{-2r_i + 11 + 24\hat{r}_i - 3\hat{r}_i\hat{r}_{i+1}}{30},$$

$$\beta_R = \frac{-2\hat{r}_{i+2} + 11 + 24r_{i+1} - 3r_{i+1}r_i}{30}. \quad (\text{B7})$$

APPENDIX C

CLUMP IDENTIFICATION

In the simulation, the nuclear gas disk fragments into many gas clumps due to self-gravitational instability. To analyze the individual and statistical properties of the gas clumps, we identify each gas clumps using a clump find program. In this appendix, we explain our identification method.

We assume that a cell (i,j) is eligible for being contained in a gas clump if the cell satisfies the following two conditions: (1) $\Sigma_{i,j} > \Sigma_{\text{th,clump}}$, and (2) $T_{i,j} < T_{\text{th,clump}}$. We define a gas clump as a group of cells that satisfy the two conditions and are each adjacent to one of the other clump members. This clump identification method is similar to the friend-of-friend (FOF) algorithm in which the linking length is taken to be the grid size. To avoid detection of transient objects, we remove from the analysis result the gas clumps of which the number of the members is less than $n_{\text{th,clump}}$. In this study, we assume $\Sigma_{\text{th,clump}} = 5 \times 10^3 M_\odot \text{pc}^{-2}$, $T_{\text{th,clump}} = 50 \text{ K}$, and $n_{\text{th,clump}} = 9$.

REFERENCES

- Alard, C. 2001, *A&A*, **379**, 44
 Bigiel, F., Leroy, A., Walter, F., Brinks, E., de Block, W., Madore, B., & Thornley, M. 2008, *AJ*, **136**, 2846
 Binney, J., Gerhard, O., Stark, A., Bally, J., & Uchida, K. 1991, *MNRAS*, **252**, 210

- Binney, J., & Tremaine, S. 1987, *Galactic Dynamics* (Princeton, NJ: Princeton Univ. Press)
- Bonnell, I., & Rice, W. 2008, *Science*, **321**, 1060
- Buta, R., & Crocker, D. 1993, *AJ*, **105**, 1344
- Christopher, M., Scoville, N., Stolovy, S., & Yun, M. 2005, *ApJ*, **622**, 346
- Coil, A., & Ho, P. 1999, *ApJ*, **513**, 752
- Coil, A., & Ho, P. 2000, *ApJ*, **533**, 245
- Dame, T., Elmegreen, B., Cohen, R., & Thaddeus, P. 1986, *ApJ*, **305**, 892
- Debattista, V., & Shen, J. 2007, *ApJ*, **654**, 127
- Donovan, J. L., Herrnstein, R. M., & Ho, P. T. 2006, *ApJ*, **647**, 159
- Eisenhauer, F., Schödel, R., Genzel, R., Ott, T., Tecza, M., Abuter, R., Eckart, A., & Alexander, T. 2003, *ApJ*, **597**, 121
- El-Zant, A., & Shlosman, I. 2003, *ApJ*, **595**, L41
- Englmaier, P., & Shlosman, I. 2004, *ApJ*, **617**, L115
- Erwin, P. 2004, *A&A*, **415**, 941
- Erwin, P., & Sparke, L. 2002, *AJ*, **124**, 65
- Figer, D. 2003, in *IAU Symp.* 212, *A Massive Star Odyssey: From Main Sequence to Supernova*, ed. K. van der Hucht, A. Herrero, & C. Esteban (San Francisco, CA: ASP), 487
- Figer, D., Kim, S., Morris, M., Serabyn, E., Rich, R., & Mclean, I. 1999, *ApJ*, **525**, 750
- Friedli, D. 1996, *A&A*, **312**, 761
- Friedli, D., & Martinet, L. 1993, *A&A*, **277**, 27
- Fukunaga, M. 1983, *PASJ*, **35**, 173
- Fukunaga, M. 1984, *PASJ*, **36**, 433
- Fukunaga, M., & Tosa, M. 1989a, *PASJ*, **41**, 241
- Fukunaga, M., & Tosa, M. 1989b, *PASJ*, **41**, 975
- Gammie, C. F., Ostriker, J. P., & Jog, C. J. 1991, *ApJ*, **378**, 565
- Gaume, R., Claussen, M., de Pree, C., Goss, W., & Mehringer, D. 1995, *ApJ*, **449**, 663
- Genzel, R., Eisenhauer, F., & Gillessen, S. 2010, *Rev. Mod. Phys.*, **82**, 3121
- Genzel, R., Thatte, N., Krabbe, A., Kroker, H., & Tacconi-Garman, L. 1996, *ApJ*, **472**, 153
- Genzel, R., et al. 2003, *ApJ*, **594**, 812
- Gerritsen, J. P., & Icke, V. 1997, *A&A*, **325**, 972
- Ghez, A., et al. 2003, *ApJ*, **586**, L127
- Ghez, A., et al. 2008, *ApJ*, **689**, 1044
- Gillessen, S., Eisenhauer, F., Fritz, T., Bartko, H., Dodds-Eden, K., Pfuhl, O., Ott, T., & Genzel, R. 2009a, *ApJ*, **707**, L114
- Gillessen, S., Eisenhauer, F., Trippe, S., Alexander, T., Genzel, R., Martins, F., & Ott, T. 2009b, *ApJ*, **692**, 1075
- Habing, H. 1968, *Bull. Astron. Inst. Neth.*, **19**, 421
- Heller, C., Shlosman, I., & Athanassoula, E. 2007, *ApJ*, **657**, L65
- Heller, C., Shlosman, I., & Englmaier, P. 2001, *ApJ*, **553**, 661
- Herrnstein, R., & Ho, P. 2002, *ApJ*, **579**, 83
- Herrnstein, R., & Ho, P. 2003, *Astron. Nachr.*, **324**, 583
- Herrnstein, R., & Ho, P. 2005, *ApJ*, **620**, 287
- Hobbs, A., & Nayakshin, S. 2009, *MNRAS*, **394**, 191
- Hockney, R., & Eastwood, J. 1988, *Computer Simulation Using Particles* (New York: Taylor & Francis Group)
- Jog, C. J., & Ostriker, J. P. 1988, *ApJ*, **328**, 404
- Kennicutt, R. C. 1998, *ApJ*, **498**, 541
- Kim, K. H., & Kim, C. 2005a, *J. Comput. Phys.*, **208**, 570
- Kim, K. H., & Kim, C. 2005b, *J. Comput. Phys.*, **208**, 527
- Krumholz, M. R., & McKee, C. F. 2005, *ApJ*, **630**, 250
- Krumholz, M. R., & Tan, J. C. 2007, *ApJ*, **654**, 304
- Launhardt, R., Zylka, R., & Mezger, P. 2002, *A&A*, **384**, 112
- Lee, C. W., Lee, H., Ann, H., & Kwon, K. 1999, *ApJ*, **513**, 242
- Lee, S., Pak, S., Davis, C. J., Herrnstein, R. M., Geballe, T., Ho, P. T., & Wheeler, J. C. 2003, *MNRAS*, **341**, 509
- Lee, S., et al. 2008, *ApJ*, **674**, 247
- Levin, Y., & Beloborodov, A. M. 2003, *ApJ*, **590**, L33
- Maciejewski, W., & Sparke, L. 1997, *ApJ*, **484**, 117
- Maciejewski, W., & Sparke, L. 2000, *MNRAS*, **313**, 745
- Maciejewski, W., Teuben, P., Sparke, L., & Stone, J. 2002, *MNRAS*, **329**, 502
- Maoz, E., & McKee, C. 1998, *ApJ*, **494**, 218
- Mapelli, M., Hayfield, T., Mayer, L., & Wadsley, J. 2008, arXiv:0805.0185
- Mcgray, R., Coil, A., & Ho, P. 2001, *ApJ*, **559**, 326
- McGray, R. S., & Ho, P. T. 2002, *ApJ*, **577**, 757
- Mezger, P. G., Duschl, W. J., & Zylka, R. 1996, *ARA&A*, **7**, 289
- Montero-Castaño, M., Herrnstein, R. M., & Ho, P. T. 2009, *ApJ*, **695**, 1477
- Morris, M. 1993, *ApJ*, **408**, 496
- Morris, M., & Serabyn, E. 1996, *ARA&A*, **34**, 645
- Namekata, D., Habe, A., Matsui, H., & Saitoh, T. R. 2009, *ApJ*, **691**, 1525
- Nayakshin, S., Cuadra, J., & Springel, V. 2007, *MNRAS*, **379**, 21
- Nishiyama, S., Nagata, T., & IRSF/SIRIUS Team. 2006, *J. Phys.: Conf. Ser.*, **54**, 62
- Nishiyama, S., et al. 2005, *ApJ*, **621**, 105
- Oka, T., Hasegawa, T., Sato, F., Tsuboi, M., Miyazaki, A., & Sugimoto, M. 2001, *ApJ*, **562**, 348
- Press, W. H., Flannery, B. P., Teukolsky, S. A., & Vetterling, W. T. 1992, *Numerical Recipes in Fortran 77: The Art of Scientific Computing*, Vol. 1 (2nd ed.; Cambridge: Cambridge Univ. Press)
- Rautiainen, P., Salo, H., & Laurikainen, E. 2002, *MNRAS*, **337**, 1233
- Sanders, R. 1998, *MNRAS*, **294**, 35
- Sawada, T., Hasegawa, T., Handa, T., & Cohen, R. 2004, *MNRAS*, **349**, 1167
- Scoville, N., Yun, M. S., Clemens, D., Sanders, D., & Waller, W. 1987, *ApJS*, **63**, 821
- Serabyn, E., & Morris, M. 1995, *Nature*, **382**, 15
- Shaw, M., Combes, F., Axon, D., & Wright, G. 1993, *A&A*, **273**, 31
- Shen, J., & Dibattista, V. P. 2009, *ApJ*, **690**, 758
- Shetty, R., & Ostriker, E. C. 2008, *ApJ*, **684**, 978
- Shlosman, I., Frank, J., & Begelman, M. 1989, *Nature*, **338**, 45
- Shlosman, I., & Heller, C. 2002, *ApJ*, **565**, 921
- Shu, C.-W. 1988, *SIAM J. Sci. Stat. Comput.*, **9**, 1073
- Shukla, H., Yun, M., & Scoville, N. 2004, *ApJ*, **616**, 231
- Solomon, P., Rivolo, A., Barrett, J., & Yahil, A. 1987, *ApJ*, **319**, 730
- Spaans, M., & Norman, C. A. 1997, *ApJ*, **483**, 87
- Stark, A. A., Gerhard, O. E., Binney, J., & Bally, J. 1991, *MNRAS*, **248**, 14
- Stole, A., Ghez, A., Lu, M. M. J., Brandner, W., & Matthews, K. 2009, *Astro-phys. Space Sci.*, **324**, 137
- Stole, A., Ghez, A., Morris, M., Lu, J., Brandner, W., & Matthews, K. 2008, *ApJ*, **675**, 1278
- Šubr, L., Schovancová, J., & Kroupa, P. 2009, *A&A*, **496**, 695
- Tosa, M., & Fukunaga, M. 1986, *PASJ*, **38**, 335
- Wada, K. 2002, *ApJ*, **566**, L21
- Wada, K., & Habe, A. 1992, *MNRAS*, **258**, 82
- Wada, K., & Norman, C. A. 2001, *ApJ*, **547**, 172
- Wada, K., Papadopoulos, P. P., & Spaans, M. 2009, *ApJ*, **702**, 63
- Wardle, M., & Yusef-Zadeh, F. 2008, *ApJ*, **683**, L37
- Wright, M. C., Coil, A. L., McGray, R. S., Ho, P. T., & Harris, A. I. 2001, *ApJ*, **551**, 254
- Yoon, S.-H., Kim, C., & Kim, K.-H. 2008, *J. Comput. Phys.*, **227**, 6001
- Yusef-Zadeh, F., Muno, M., Wardle, M., & Lis, D. 2007, *ApJ*, **656**, 847